Knotting Plasma

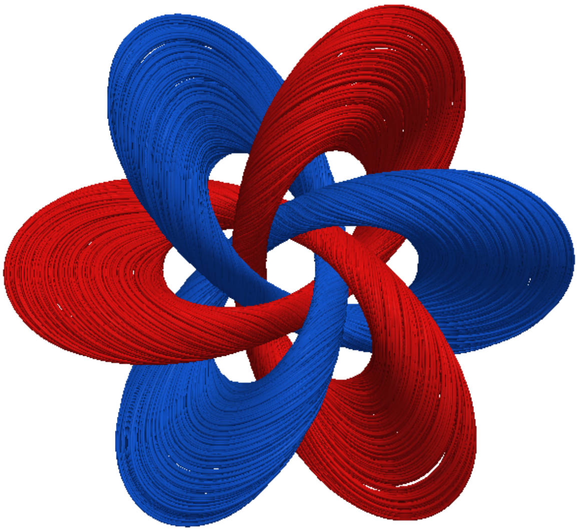

THESIS

submitted in partial fulfillment of the
requirements for the degree of

BACHELOR OF SCIENCE
in
PHYSICS

Author :	Pieter Bouwmeester
Student ID :	1153897
Supervisor :	Prof.dr. Dirk Bouwmeester
2^{nd} corrector :	Dr. Wolfgang Löffler

Leiden, The Netherlands, June 26, 2018

Knotting Plasma

Pieter Bouwmeester

Instituut-Lorentz, Leiden University
P.O. Box 9500, 2300 RA Leiden, The Netherlands

June 26, 2018

Abstract

We simulated the time evolution of plasma torus knots in resistive, viscous MHD. These torus knots are stationary solutions to the ideal MHD equations, as proposed by Kedia et al. These magnetic fields are parameterised by the winding numbers n_p and n_t and exist of several families of nested magnetic fields around a core field line. In ideal MHD, the topological structure of these solitons is conserved and these fields form stationary solutions, but these properties are not carried over to resistive MHD. We will look at the structure of the magnetic field of such a plasma.

We find that a new magnetic surface family arises whose topology depends on the poloidal winding number n_p of the initial magnetic field. The time evolution of the corresponding magnetic energy and helicity is strongly influenced by these n_p. When $n_p > 1$, the new magnetic surfaces have a non-zero Euler characteristic and depend on a zero magnetic field line along the z-axis. The toroidal winding number n_t is of lesser influence, and the corresponding zero line contracts and disappears. Both the old and the new structures are preserved over time and we observe the formation of magnetic islands between magnetic surfaces.

Contents

Version of June 26, 2018– Created June 26, 2018 - 13:50

Version of June 26, 2018– Created June 26, 2018 - 13:50

Chapter 1

Introduction

1.1 Knots in physics

Figure 1.1: *A trefoil knot*

For centuries, knots have been able to capture human interest and fascination. Ancient legends, such as that of Alexander the Great and the Gordian Knot, show that even thousands of years ago great importance was placed in the art of (un)tying. According to legend, Alexander was able to solve his problem by one powerful swing of his sword[*], modern scientist have to rely on less crude methods to solve the problems that knots present them. The knots one encounters in modern research are also substantially different from 'normal' knots in two ways. When tying a shoelace, the objective is to tie two ends of a string together, while mathematical knots are closed loops to begin with. Often these loops are in such a set-up that it is not possible for the strings to be separated without cutting at least one of the strings, such as with two interlinked loops. One loop itself is also called knotted if it is not possible to rearrange it to form a circle without cutting it. The most simple example is perhaps the trefoil knot, such as seen in figure 1.1. Also, while in the mathematical study of knots only one piece of string has to be considered at a time, while in vector fields, the whole configuration, including all field lines, has to be taken into account simultaneously.

While modern knot theory is in principle a part of the abstract mathemati-

---

[*] This statement is considered controversial [1] but a comprehensive exposition on this subject falls outside the scope of this thesis.

cal field of topology, it finds applications in a wide range of modern fields of physics. Fluid dynamics [2], liquid crystals [3], optics [4–6], quantum field theory [7] and topological quantum computation [8] are a few of the examples where the study of knot theory intertwines with contemporary physics research.

1.2 Electromagnetic Fields

The physics electromagnetism has been studied for centuries. The ancient Greek already described the effects of statically charged amber, which they called *elektrum*. The behaviour of electromagnetic fields is described by the Maxwell equations. In dimensionless units, where $c = \mu = \varepsilon_0 = 1$, the equations are given as follows:

$$\begin{aligned} \nabla \cdot \mathbf{E} &= \rho, & \nabla \cdot \mathbf{B} &= 0, \\ \nabla \times \mathbf{E} &= -\frac{\partial \mathbf{B}}{\partial t}, & \nabla \times \mathbf{B} &= \mathbf{J} + \frac{\partial \mathbf{E}}{\partial t}. \end{aligned}$$

Here $\mathbf{E}$ is the electric field, $\mathbf{B}$ is the magnetic field, while ρ is the charge density and $\mathbf{J}$ is the current density. Since $\nabla \cdot \mathbf{B} = 0$, one can define a vector potential $\mathbf{A}$ such that $\nabla \times \mathbf{A} = \mathbf{B}$. The vector potential is not unique, since adding a term $\nabla\Phi$ to a potential $\mathbf{A}$ still gives us $\nabla \times (\mathbf{A} + \nabla\Phi) = \nabla \times \mathbf{A} = \mathbf{B}$. However, in general we will take Φ to be equal to zero.

1.3 Fluid Dynamics

Fluid dynamics is the study of the macroscopic properties of an uncharged fluid. Both liquids and gasses are considered fluids, as a fluid is usually defined as a substance that can be rearranged without changing the macroscopic properties of the fluid citebatchelor2000introduction. This in contrast to a solid, that can only change shape under influence of external conditions. This definition is not rigorous, and many materials have some properties of fluids, and some properties of solids. An example might be the famous pitch experiment [9]. Pitch is generally considered a solid, but this experiment shows it to deform liquid like on timescales in the order of years.

1.3.1 Mechanical Equilibrium

Solid bodies are in equilibrium when the total force and couple acting on the body are zero. When considering fluids, different elements of a single object are able to move relative to each other, making it harder to find an equilibrium. The total force acting on a fluid in a volume V is given by

$$\int_V \mathbf{F} \mathrm{d}^3 x, \tag{1.1}$$

where **F** is the position depend force. When the fluid is at rest, the surrounding matter at the surface A bounding V exerts a force due to the pressure p which we can write as

$$-\int p \cdot \mathrm{d}^2 \mathbf{A} = \int_V \nabla p \mathrm{d}^3 x \tag{1.2}$$

by the scalar divergence theorem. So a fluid is in equilibrium when

$$\int_V (\mathbf{F} - \nabla p) \mathrm{d}^3 x = 0. \tag{1.3}$$

If both **F** and ∇p are continuously dependent on position, we can write the necessary condition for equilibrium to be

$$\mathbf{F} = \nabla p. \tag{1.4}$$

1.3.2 Eulerian and Lagrangian Specification

The velocity of a fluid is an important quantity when describing fluid dynamics. There are two distinctly different possibilities of describing this, called the Eulerian and Lagrangian velocity. The Eulerian velocity **u** specifies the velocity of a fluid as function of position and time, akin to the electromagnetic field. The Eulerian velocity provides us with the velocity field at each moment. The Lagrangian velocity **v** tracks the movement of the infinitesimal small parts of the fluid. It identifies each part of the fluid by its starting position a at a certain time t_0 and gives the velocity of this part at a general time t.

Both specifications have their uses in the study of fluid dynamics, but in this thesis we will mainly use the Eulerian specification **u**, unless otherwise noted. The Lagrangian specification is more cumbersome when analysing velocity fields and is not able to directly give the spatial gradient of velocity in fluids. To study the acceleration of a fluid element in terms of the Eulerian velocity, one then has to use the material derivative

$$\frac{\mathrm{D}}{\mathrm{D}t} = \frac{\partial}{\partial t} + \mathbf{u} \cdot \nabla. \tag{1.5}$$

So we get that $\frac{\partial \mathbf{v}}{\partial t} = \frac{\mathrm{D}\mathbf{u}}{t}$. Whether one uses the normal time derivative or the material derivative is whether we are interested in the local rate of change of a quantity, or the rate of change of a quantity in the frame of the moving fluid.

1.3.3 The Continuity Equation

Consider a closed surface A with a fixed position, i.e. it does not move with the fluid flow, enclosing a volume V. The total mass of the fluid in V is given by $\int_V \rho \mathrm{d}^3 x$. Barring sources or sinks, the net rate of change of the fluid mass is given by $\int \rho \mathbf{u} \cdot \mathrm{d}^2\mathbf{A}$, the net rate at which mass flows out of the boundary. Conservation of mass is thus given when

$$\frac{\mathrm{d}}{\mathrm{d}t}\int_V \rho \mathrm{d}^3 x = -\int \rho \mathbf{u} \cdot \mathrm{d}^2\mathbf{A}. \tag{1.6}$$

Since the volume is fixed in space, we can rewrite the left hand of this equation by differentiation under the integral sign with the partial time derivative. Using the divergence theorem on the right hand of equation 1.6, we can write

$$\int_V \frac{\partial \rho}{\partial t} + \nabla \cdot (\rho \mathbf{u}) \mathrm{d}^3 x = 0 \tag{1.7}$$

for all V. Since this result holds for all V, we find the *continuity equation*

$$\boxed{\frac{\partial \rho}{\partial t} + \nabla \cdot (\rho \mathbf{u}) = 0.} \tag{1.8}$$

This equation ensures that no mass is gained or lost, all changes in mass in a infinitesimal volume correspond to a mass flow through the border.

1.4 Helicity and Linkedness

Although knot theory has found a place in physics, it might not be immediately obvious how the study of plasma's has anything to do with knots. Of course, magnetic field lines might be tangled a bit, but that alone does not imply any meaningful connection is there. The answer lies in the *helicity* h_m of the magnetic field. The helicity is defined as

$$h_m = \int_V \mathbf{A} \cdot \mathbf{B} \mathrm{d}^3 x \tag{1.9}$$

which we will show to be constant in certain plasma models in section 2.1.2. Helicity is directly related to the knottedness of a plasma. This is the most obvious when considering a configuration of exactly two thin closed magnet linked rings. If both rings carry a constant flux Φ_1 and Φ_2 and have no twist, we can calculate the helicity of the system by integrating equation 1.9 over both rings. Integrating the first ring in the direction of the magnetic field gives $\int_{V_1} \mathbf{B} \cdot \mathrm{d}\mathbf{a} = \Phi_1$. Using that $\nabla \times \mathbf{A} = \mathbf{B}$ and Stokes theorem, we now get the helicity of the first ring as

$$\begin{aligned} h_m &= \int_{V_1} \mathbf{A} \cdot \mathbf{B} \mathrm{d}^3 x && (1.10) \\ &= \Phi_1 \oint_C \mathbf{A} \cdot \mathrm{d}\mathbf{l} && (1.11) \\ &= \Phi_1 \int_S \mathbf{B} \cdot \mathrm{d}\mathbf{a} && (1.12) \\ &= \Phi_1 \Phi_2. && (1.13) \end{aligned}$$

Here, we used that the the flux passing through the surface bounded by the first ring is exactly the flux of the second ring. It follows that the helicity of the whole system is then given by $2\Phi_1\Phi_2$.

The above is probably the single simplest system one can imagine having a non-zero helicity. However, it still has some value to talk about some concepts. First, it should be clear that if the two rings above were *not* linked, the flux through the surfaces bounded by the rings disappears, giving a total helicity of zero. Second, in a system where two rings are not simply linked, but are linked n times, helicity would go up proportionally with n. Third, when one adds more rings, and starts linking them, the final helicity would be the sum of the helicity due two any two connected components. This also means that a zero helicity *does not* imply no linkage. One can link two rings to a third, but not each other in such a way that the helicity due to the first ring counteracts the helicity due to the second. A more rigorous treatment of helicity is covered in section 2.1.2.

1.4.1 Writhe and Twist

Above, we only considered the case where the field lines on the rings were not twisted. One can think about writhe as the curving of the central field line and twist as the rotation of the ring about the center line. Writhe and twist are both variant, but the total contribution of both to helicity is constant in ideal MHD [10].

Chapter 2

MHD Theory

Magnetohydrodynamics, or MHD, is the model that describes the macroscopic properties of plasma. The most simplified version of MHD models a plasma as a single fluid with no electrical resistance and no other kinetic effects. Although real world plasma's often don't adhere to these constraints, for instance having a small, but non-zero, resistance, ideal MHD is often used in the study of nuclear fusion reactors. Finding stable equilibrium states in ideal MHD is an important step in the realisation of such a reactor. Since a plasma can be described as a fluid of charged particles, we will start with an introduction to fluid dynamics before we describe the models of (ideal) MHD.

2.1 Ideal MHD

2.1.1 Governing Equations

We know from the laws of Newton that $\mathbf{F} = m\mathbf{a}$, the acceleration of an object is equal to the force that acts upon it divided by it's mass. In MHD, this takes the form of the *momentum equation*

$$\mathbf{F} = \rho \frac{\mathrm{D}\mathbf{u}}{\mathrm{D}t}. \tag{2.1}$$

The two forces we consider here are the Lorentz force and the force due to pressure. The Lorentz force is given by $\mathbf{F}_l = \mathbf{j} \times \mathbf{B}$, with $\mathbf{j}$ the current. The force due to a pressure p is given by $\mathbf{F}_p = -\nabla p$. These are the only forces we consider in ideal MHD and we expand equation 2.1 where $\mathbf{F} = \mathbf{F}_l + \mathbf{F}_p$. The momentum equation is then of the form

$$\boxed{\rho\frac{\partial \mathbf{u}}{\partial t} + \rho\mathbf{u}\cdot\nabla\mathbf{u} - \mathbf{J}\times\mathbf{B} + \nabla p = 0.} \tag{2.2}$$

Ohm's Law for a plasma is given by

$$\mathbf{E} + \mathbf{u}\times\mathbf{B} = \frac{\mathbf{J}}{\sigma} \tag{2.3}$$

where σ is the conductivity of the plasma. In ideal MHD, which we model to be restive free, we take the limit $\sigma \to \infty$. In this case the right hand side of equation 2.3 disappears. Using the laws of Maxwell, we know that $\nabla \times \mathbf{E} = -\frac{\partial B}{\partial t}$ a so when we take the curl of the left hand side of equation 2.3, we find the *induction equation* by

$$\boxed{\frac{\partial \mathbf{B}}{\partial t} - \nabla\times(\mathbf{u}\times\mathbf{B}) = 0.} \tag{2.4}$$

We will consider an isothermal, compressible plasma. Mass is conserved in this plasma, so we use the continuity equation 1.8 we found in section 1.3.3

$$\boxed{\frac{\partial \rho}{\partial t} + \nabla\cdot(\rho\mathbf{u}) = 0.} \tag{2.5}$$

Since equation 2.4 is linear and homogeneous in **B**, as well as an first order differential in t, it completely determines **B** for a given initial condition [11].

Ideal MHD models do not incorporate (electromagnetic) resistance. Therefor solutions of equations 2.2, 2.4 and 1.8 where both $\frac{\partial \mathbf{u}}{\partial t} = 0$ as $\frac{\partial \mathbf{B}}{\partial t} = 0$ are feasible. These solutions are called *stationary equilibria* and are of special interest when studying MHD

2.1.2 Conservation of Helicity

As we have seen in section 1.4, the topological structure of the magnetic field lines is correlated to the magnetic helicity h_m of the field. The helicity $h_m = \int_V \mathbf{A}\cdot\mathbf{B}\mathrm{d}^3x$ of the magnetic field is constant in time for certain conditions on **B** and **u**, which we will discuss here. The time dependency of h_m can be written as

$$\frac{\partial h_m}{\partial t} = \frac{\partial}{\partial t}\int_V \mathbf{A}\cdot\mathbf{B}\mathrm{d}^3x = \int_V \frac{\partial \mathbf{A}}{\partial t}\cdot\mathbf{B} + \mathbf{A}\cdot\frac{\partial \mathbf{B}}{\partial t}\mathrm{d}^3x. \tag{2.6}$$

By the induction equation 2.4, we can write

$$\frac{\partial \mathbf{B}}{\partial t} = \nabla \times \frac{\partial \mathbf{A}}{\partial t} = \nabla \times (\mathbf{u} \times \mathbf{B}), \tag{2.7}$$

so $\frac{\partial \mathbf{A}}{\partial t} = \mathbf{u} \times \mathbf{B}$. Using this, we find

$$\frac{\partial \mathbf{A}}{\partial t} \cdot \mathbf{B} = (\mathbf{u} \times \mathbf{B}) \cdot \mathbf{B} = 0. \tag{2.8}$$

Next to that, we also find that

$$\mathbf{A} \cdot \frac{\partial \mathbf{B}}{\partial t} = \mathbf{A} \cdot \nabla \times (\mathbf{v} \times \mathbf{B}) \tag{2.9}$$

$$= \nabla \cdot \big((\mathbf{v} \times \mathbf{B}) \times \mathbf{A}\big) - (\mathbf{v} \times \mathbf{B}) \cdot \nabla \times \mathbf{A}. \tag{2.10}$$

The right side of equation 2.10 can be rewritten as $(\mathbf{v} \times \mathbf{B}) \cdot \nabla \times \mathbf{A} = (\mathbf{v} \times \mathbf{B}) \cdot \mathbf{B} = 0$. The left side can be rewritten with the identity $(\mathbf{v} \times \mathbf{B}) \times \mathbf{A} = (\mathbf{A} \cdot \mathbf{v})\mathbf{B} - (\mathbf{A} \cdot \mathbf{B})\mathbf{v}$. Using this and equation 2.8, we van rewrite equation 2.6 as

$$\frac{\partial h_m}{\partial t} = \int_V \nabla \cdot \big((\mathbf{A} \cdot \mathbf{v})\mathbf{B} - (\mathbf{A} \cdot \mathbf{B})\mathbf{v}\big) \mathrm{d}^3 x \tag{2.11}$$

$$= \oint_S \big((\mathbf{A} \cdot \mathbf{v})\mathbf{B} - (\mathbf{A} \cdot \mathbf{B})\mathbf{v}\big) \cdot \mathrm{d}\hat{\mathbf{n}}. \tag{2.12}$$

Here the second line is found using the divergence theorem, with S the border of V and $\hat{\mathbf{n}}$ the normal of that border. We find that if both $\mathbf{B} \cdot \mathbf{n} = 0$ as well as $\mathbf{v} \cdot \mathbf{n} = 0$, helicity is conserved. One instance of this is found in flux tubes, where $\mathbf{B} \cdot \mathbf{n} = 0$. One can choose a surface $S(t)$ that moves in time with the plasma fluid. In this case helicity will be preserved. An other example would be when we consider a local plasma configuration. The magnetic field and the fluid field will go to zero on great distances from this configuration. In this case the helicity of the whole configuration will be preserved.

2.1.3 Force Free and Force Balanced solutions

In *force free MHD*, equations 2.2 and 2.4 are solved with fields that adhere to the force free condition [12]:

$$\mathbf{J} \times \mathbf{B} = (\nabla \times \mathbf{B}) \times \mathbf{B} = 0. \tag{2.13}$$

Cosmic magnetic fields often satisfy this condition [13]. These cosmic magnetic fields often form around stars, and result in large magnetic fields in the low density space around these stars. When this is the case, the Lorentz force vanishes and the motion of plasma will not depend on the magnetic field, allowing for a stationary equilibrium. Adhering to condition 2.13 ensures that the magnetic field lines are parallel to their own curl [12], i.e.

$$\nabla \times \mathbf{B} = \alpha \mathbf{B} \tag{2.14}$$

with α dependent on position.

In *force balanced MHD*, one searches for solutions where $\mathbf{J} \times \mathbf{B} = \nabla p$. In this case the magnetic force exactly negates the pressure gradient force. Solutions of the ideal MHD equations with this property form *static* equilibria [14]. These are equilibria where $\mathbf{u} = 0$ everywhere.

2.1.4 Exact stationary solution

In 1956, Chandrasehkar considered an other equilibrium in ideal MHD with an incompressible fluid [15]. A fluid is incompressible when the density of each mass element is constant, i.e.

$$\frac{\mathrm{D}\rho}{\mathrm{D}t} = 0. \tag{2.15}$$

In this case, one can expand the continuity equation 1.8 to write

$$\begin{aligned} \frac{\partial \rho}{\partial t} + \nabla \cdot (\rho \mathbf{u}) &= \frac{\partial \rho}{\partial t} + \mathbf{u} \cdot \nabla \rho + \rho \nabla \cdot \mathbf{u} && (2.16) \\ &= \frac{\mathrm{D}\rho}{\mathrm{D}t} + \rho \nabla \cdot \mathbf{u} && (2.17) \\ &= \rho \nabla \cdot \mathbf{u} = 0. && (2.18) \end{aligned}$$

Thus with non zero density, we find that $\nabla \cdot \mathbf{u} = 0$. A solution of the ideal MHD equations is then given by

$$\mathbf{u} = \pm \frac{\mathbf{B}}{\sqrt{\rho}}, \qquad p + \frac{B^2}{2} = p_\infty, \tag{2.19}$$

with p_∞ constant. To show that 2.19 is a solution of the incompressible MHD equations, we will have to show that equations 2.2 and 2.4 still hold. Given that the plasma has no net charge, we use $\mathbf{J} = \nabla \times \mathbf{B}$ to write

$$(\mathbf{J} \times \mathbf{B}) = (\nabla \times \mathbf{B}) \times \mathbf{B} = -\frac{1}{2} \nabla B^2 + \mathbf{B} \cdot \nabla \mathbf{B}. \tag{2.20}$$

Now we can write equation 2.2 as

$$\rho \left(\frac{\partial \mathbf{u}}{\partial t} + \mathbf{u} \cdot \nabla \mathbf{u} \right) - \mathbf{B} \cdot \nabla \mathbf{B} + \nabla \left(p + \frac{B^2}{2} \right) = 0. \tag{2.21}$$

From the stationary condition 2.19, the last term of equation 2.21 is the gradient of a constant and thus zero. Next to that, since we consider an incompressible plasma, the terms $\mathbf{u} \cdot \nabla \mathbf{u}$ and $\mathbf{B} \cdot \nabla \mathbf{B}$ cancel each other. We conclude that $\frac{\partial u}{\partial t} = 0$. Also, since $\mathbf{u}$ and $\mathbf{B}$ are pointed in the same direction, the induction equation 2.4 gives us that

$$\frac{\partial \mathbf{B}}{\partial t} - \nabla \times (\mathbf{u} \times \mathbf{B}) = \frac{\partial \mathbf{B}}{\partial t} = 0. \tag{2.22}$$

With both $\frac{\partial \mathbf{u}}{\partial t} = 0$ as $\frac{\partial \mathbf{B}}{\partial t} = 0$, equation 2.19 is a stationary solution of the ideal MHD equations, and was dubbed the *exact stationary solution*

2.2 non-ideal MHD

While ideal MHD is a suitable way to approximate the behaviour of a plasma, it is not complete. Several phenomena such as electric resistance, radiation, viscosity, temperature variation and (self) gravity are not included in the ideal MHD model. The effect of resistiviy and viscosity will be studied in this paper, by adding the to the ideal MHD model. These effects are those of the current resistance and the viscosity. We don't include gravity, as it is believed that the effects due to gravitational attraction are several orders of magnitude smaller then the other forces in play. In this case, we take our plasma to be isothermal, and do not account for any external influences.

2.2.1 Resistivity

While we want to model the effect of non-zero resistance and viscosity, we don't need the associated forces to be very big before we see results. In fact, even a small resistance makes it so that we cannot use $\int \mathbf{A} \cdot \mathbf{B} \mathrm{d}^3 x$ as integral of motion. Because of this, the motion of plasma is not confined to the lines of the magnetic field [16] and where magnetic field lines were not allowed to break in ideal MHD, this property does not translate to resistive MHD. Here we will see that these lines are allowed to break and reconnect locally, changing the topological structure of the field. The higher the resistivity, the more pronounced this effect will be.

Introducing resistivity in the MHD-equations gives us $\mathbf{E}_{\text{res}} = \eta \mathbf{J}$. When η is constant in space, this alters the induction equation 2.4 to

$$\frac{\partial \mathbf{B}}{\partial t} = \nabla \times (\mathbf{u} \times \mathbf{B}) - \nabla \times \big(\eta (\nabla \times \mathbf{B})\big) \tag{2.23}$$

$$= \nabla \times (\mathbf{u} \times \mathbf{B}) + \eta \nabla^2 \mathbf{B}. \tag{2.24}$$

This change in the induction equation is the reason why we lose the conservation of helicity. We can see this, when expanding the two terms in integral 2.6. We find that

$$\frac{\partial \mathbf{A}}{\partial t} \cdot \mathbf{B} = -\eta(\nabla \times \mathbf{B}) \cdot \mathbf{B} \tag{2.25}$$

and

$$\mathbf{A} \cdot \frac{\partial \mathbf{B}}{\partial t} = -\mathbf{A} \cdot \eta(\nabla \times \mathbf{B}) \tag{2.26}$$

which are both non-zero in general. However, since $\frac{\partial h_m}{\partial t}$ is linear in η, small values of η should give a small change in helicity. In this case, while the topological structure of the magnetic field will decay, it strongly constrains the relaxation of the magnetic field and does put a bound on the decay of the magnetic energy.

2.2.2 Viscosity

The viscous force F_{visc} in general is anisotropic and is usually represented by a tensor. However, viscosity strongly influences the behaviour of gasses, fluids and plasma. The detailed study of viscosity on liquids is a rich and diverse field of study, but unfortunately falls outside the scope of this thesis. Nevertheless, we can not completely ignore viscosity and we will assume that we can approximate it using a scalar constant ν. We write the viscous force as

$$\mathbf{F}_{\text{visc}} = -\rho\nu\nabla^2\mathbf{u}. \tag{2.27}$$

Adding viscosity to equation 2.2, we find that the following resistive momentum equation to solve

$$\rho\left(\frac{\partial \mathbf{u}}{\partial t} + \mathbf{u} \cdot \nabla\mathbf{u}\right) - \mathbf{B} \cdot \nabla\mathbf{B} + \nabla\left(p + \frac{B^2}{2}\right) + \rho\nu\nabla^2\mathbf{u} = 0. \tag{2.28}$$

2.3 Numerical Methods

Solving resistive MHD equations analytically is a daunting task, if possible at all, for most boundary constraints. The resistive induction equation 2.24 and the viscous momentum equation 2.28 do not generally allow for easy solutions. Finding solutions this way is feasible when problems are, for example, simplified by several symmetries. For studying more complex plasma structures, one has to solve the full MHD equations 1.8, 2.24 and 2.28 numerically.

2.3.1 The PENCIL code

Several different codes specialised in solving MHD equations have been developed in the past few decades. For this thesis we used the PENCIL-code [17]. The PENCIL-code does not directly calculate $\mathbf{B}$, but solves the relevant MHD equations in terms of the vector potential $\mathbf{A}$, only calculating thge magnetic field using by $\mathbf{B} = \nabla \times \mathbf{A}$. This ensures that $\nabla \cdot \mathbf{B} = 0$, even when numerical errors start to accumulate. If $\mathbf{B}$ was the variable solved for, then these numerical errors could lead to a non-zero $\nabla \cdot \mathbf{B}$ term, which is physically unfeasible. The density ρ is calculated in terms of $\ln(\rho)$. The magnetic vector potential here is chosen with the Weyl gauge, i.e. the scalar component Φ of the potential is zero.

The PENCIL Code is unit agnostic and uses dimensionless quantities. This has consequence that the actual quantities calculated by the PENCIL code depend on our choice of units for the magnetic permeability and the speed of sound c_s, for these are both set hardcoded 1. The PENCIL code is capable of handling viscosity and resistivity. Resistivity is always a scalar quantity, but it calculates viscosity using the viscosity tensor $\mathbf{S}$. Thus the PENCIL code solves for the following formula:

$$\frac{\mathrm{D}}{\mathrm{D}t} \ln \rho = -\nabla \cdot \mathbf{u}, \tag{2.29}$$

$$\frac{\partial}{\partial t} \mathbf{A} = \mathbf{u} \times \mathbf{B} - \eta \mathbf{j}, \tag{2.30}$$

$$\frac{\mathrm{D}}{\mathrm{D}t} \mathbf{u} = \frac{1}{\rho} \left(-\nabla p + \mathbf{j} \times \mathbf{B} + \mathbf{F}_{\mathrm{visc}} \right). \tag{2.31}$$

The first equations are respectively the continuity equation 1.8 and the induction equation 2.24 in terms of $\mathbf{A}$ and $\ln \rho$. The last equation is a more general version of the viscous momentum equation 2.28. In section 2.2.2, we expressed $\mathbf{F}_{\mathrm{visc}}$ as a force dependent on a viscous scalar constant ν. but the PENCIL code actually calculates it using the divergence of the traceless rate of strain tensor $\mathbf{S}$ given by $S_{ij} = \frac{1}{2} \left(\frac{\partial u_i}{\partial x_j} + \frac{\partial u_j}{\partial x_i} \right) - \frac{1}{3} \delta_{ij} \nabla \cdot \mathbf{u}$. $\mathbf{F}_{\mathrm{visc}}$ is then defined using $\mathbf{S}$ as

$$\mathbf{F}_{\mathrm{visc}} = 2 \nabla \cdot (\nu \rho \mathbf{S}). \tag{2.32}$$

2.3.2 constants

The PENCIL code allows us to choose the values for ν and η. We take them both to be constant in time and they are set to $\nu = \eta = 2 \cdot 10^{-4}$. The Magnetic Prandtl number $\mathrm{Pr}_{\mathrm{m}} = \frac{\nu}{\eta}$ is unity in this case, which is a value that can be found in laboratories [18]. We set $p_\infty = 1$. We tried to scale the initial magnetic field strength with a factor 0.25, but for high n_p and n_t these simulations could crash if the PENCIL code was not able to resolve them. In that case we scaled the magnetic field with a factor 0.125. The simulations are done in a grid with 256^3 grid points and we simulated an isothermal plasma.

Chapter 3

MHD simulations

3.1 Initial Magnetic Field

There are several ways to construct a magnetic field with non-zero helicity. We use the construction that has been described by Kedia [19]. He uses *Bateman's construction* [20] to generate sets of knotted null-electromagnetic fields. Null-electromagnetic fields are fields where the electric and magnetic fields have the same magnitude and are orthogonal in respect to each other. According to Robinson [21], null electromagnetic fields move according to the Poynting vector $\mathbf{S} = \mathbf{E} \times \mathbf{B}$. The flield lines of the electromagnetic field move as if they flow along this Poynting field. If the electromagnetic field is continuous, this flow is continuous as well, preserving the topology of the electromagnetic field.

Bateman's construction is used to construct a family electromagnetic null fields. it uses two complex scalar functions $(\alpha(\mathbf{r}, t), \beta(\mathbf{r}, t))$ to generate this family. These functions have to satisfy the condition that

$$\mathbf{F} = \nabla\alpha \times \nabla\beta = i(\partial_t\alpha\nabla\beta - \partial_t\beta\nabla\alpha). \tag{3.1}$$

Note that if the pair (α, β) satisfies condition 3.1, then for all strictly positive integers n_t and n_p, the pair $(\alpha^{n_t}, \beta^{n_p})$ does so as well. After all, the following holds:

$$\begin{aligned}
\nabla\alpha^{n_t} \times \nabla\beta^{n_p} &= (\alpha^{n_t-1}\nabla\alpha) \times (\beta^{n_p-1}\nabla\beta) \\
&= \alpha^{n_t-1}\beta^{n_p-1}(\nabla\alpha \times \nabla\beta) \qquad (3.2) \\
&= \alpha^{n_p-1}\beta^{n_t-1}i(\partial_t\alpha\nabla\beta - \partial_t\beta\nabla\alpha) \\
&= i(\partial_t\alpha^{n_p}\nabla\beta^{n_t} - \partial_t\beta^{n_t}\nabla\alpha^{n_p}) \qquad (3.3)
\end{aligned}$$

$\mathbf{F}$ is known as the Riemann-Silberstein vector, so that $\mathbf{F} = \mathbf{E} + i\mathbf{B}$. Thus the initial magnetic field **B** will be equal to:

$$\begin{aligned}\mathbf{B} &= \frac{\mathrm{Im}(\mathbf{F})}{\sqrt{a}} \\ &= \frac{\mathrm{Im}\left[\nabla\alpha^{n_t} \times \nabla\beta^{n_p}\right]}{\sqrt{a}}\end{aligned} \tag{3.4}$$

with $n_t, n_p \in \mathbb{N}_{>0}$ and we will classify our magnetic fields by the values of n_t and n_p. We also have a normalisation constant $a = \int(\mathrm{Im}\left[\nabla\alpha^{n_t} \times \nabla\beta^{n_p}\right])$, ensuring that all the fields we study have the same magnetic energy.

We find that $\mathbf{F} \cdot \mathbf{F} = 0$ because

$$\begin{aligned}\mathbf{F} \cdot \mathbf{F} &= (\nabla\alpha \times \nabla\beta) \cdot i(\partial_t\alpha\nabla\beta - \partial_t\beta\nabla\alpha) && (3.5)\\ &= i\partial_t\alpha(\nabla\alpha \times \nabla\beta) \cdot \nabla\beta - i\partial_t\beta(\nabla\alpha \times \nabla\beta) \cdot \nabla\alpha && (3.6)\\ &= 0 && (3.7)\end{aligned}$$

Since both $\nabla\alpha$ and $\nabla\beta$ are perpendicular to $(\nabla\alpha \times \nabla\beta)$. From this it follows that both $\mathbf{E} \cdot \mathbf{B} = 0$ and $\mathbf{B}^2 = \mathbf{E}^2$, thus **B** is indeed a null magnetic field.

Following Kedia and Irvine [19], we choose α and β to be the following:

$$\alpha = \frac{r^2 - t^2 - 1 + 2iz}{r^2 - (t-i)^2} \tag{3.8}$$

$$\beta = \frac{2(x - iy)}{r^2 - (t-i)^2} \tag{3.9}$$

Not only does this pair satisfy condition 3.1, it also has some other properties. First of all, one can calculate that $|\alpha|^2 + |\beta|^2 = 1$ for all $t \in \mathbb{R}$. Next to that, at $t = 0$, this pair forms the stereographic projection from S^3 onto $\mathbb{R}^3$, with S^3 being the hypersphere in $\mathbb{R}^4$. S^3 is often expressed as $S^3 = \{(z_1, z_2) \in \mathbb{C}^2 |\, |z_1|^2 + |z_2|^2 = 1\}$ and the stereographic projection is then given by $(\alpha(z_1), \beta(z_2))$. In this case, **B** is the Kamchatnov-Hopf soliton and is defined by the Hopf map [22], a function from $\mathbb{R}^3$ to $\mathbb{C}$ where every point in $\mathbb{C}$ is mapped from a circle in $\mathbb{R}^3$. If two circles map to different points, then those two circles are linked in $\mathbb{R}^3$. A very important property of the Hopf map is that every pair of these circles is linked.

When using Bateman's construction, the magnetic vector potential is given by

$$\mathbf{A} = \frac{\mathrm{Im}[\beta^{n_p}\nabla\alpha^{n_t}]}{\sqrt{a}}. \tag{3.10}$$

To show that this is a valid vector potential, we calculate

$$\nabla \times \mathbf{A} = \frac{\mathrm{Im}[\nabla \times (\beta^{n_p} \nabla \alpha^{n_t})]}{\sqrt{a}} \tag{3.11}$$

$$= \frac{\mathrm{Im}\left[\beta^{n_p} \nabla \times \nabla \alpha^{n_t} + \nabla \alpha^{n_t} \times \nabla \beta^{n_p}\right]}{\sqrt{a}} \tag{3.12}$$

$$= \frac{\mathrm{Im}\left[\nabla \alpha^{n_t} \times \nabla \beta^{n_p}\right]}{\sqrt{a}} = \mathbf{B}. \tag{3.13}$$

We used that the curl of the gradient of a scalar disappears. We thus find that **A** is indeed the magnetic vector potential of **B**.

3.1.1 Field Structure

With our choice for α and β we find a very interesting magnetic field **B** regardless of our choices for n_t and n_p. The magnetic fields constructed in this way have a finite amount of *core field lines*. If $n_p n_t > 1$, these core field lines are closed and form (n_t, n_p)-torus lines, i.e. they lie on a torus and have a toroidal winding number n_t and poloidal winding number n_p. All the other field lines lie on nested surfaces that form tori around one of the core field line. Together, those surfaces fill all of space. In the case of $n_t n_p > 1$, each field line fills one of the surfaces by oscillating around a core field line in a periodic way. When $n_t = n_p = 1$, we saw in the previous section that **B** forms the Kamchatnov-Hopf soliton. In this case each field line is a circle linked with every other field line.

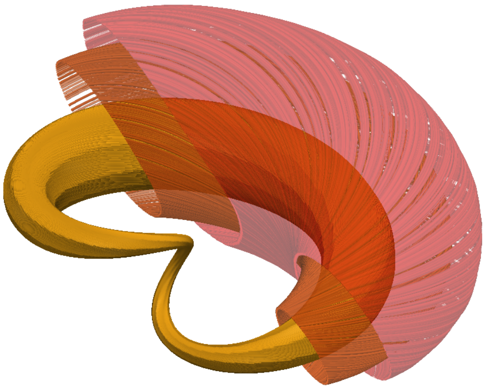

Figure 3.1: *Example of the (2,1)-magnetic field. Depicted are three field lines, each of which fills a surface around a core field line. The outer two field lines have been cut off for better visibility.*

Figure 3.1 gives an example of three field lines in the $(2, 1)$ field. The field lines lie around a –not depicted– core field line and all three field lines fill a surface. The three surfaces are nested. The whole of space is filled by families of nested surfaces. Note that there are different families of nested field lines. There is one family of nested surfaces of field lines lying around each of the different core field lines.

The parameters n_t and n_p define the topology of the field and the way that the core field lines are linked with each other. Since the rest of the field depends on this linking, we shall examine the core field lines in more detail.

When $n_p n_t > 1$, the initial core field lines are closed field lines and are intertwined to form (n_t, n_p) knots, with n_t toroidal windings and n_p poloidal winding. In the initial field, these field lines are positioned in such a way that one could draw a torus in such a way that all the core field lines lie on it's surface. The amount of core field lines is given by $2n_g = 2 \cdot \gcd(n_t, n_p)$.

The helicity h_m of all the (n_t, n_p)-knots is non-zero. Furthermore, the helicity is not only dependent on the 'linkedness' of the field, but also on the magnetic field strength. Recall that $h_m = \int \mathbf{A} \cdot \mathbf{B} \mathrm{d}V$. Since $\mathbf{B} = \nabla \times \mathbf{A}$, we have $\mathbf{A} \sim \mathbf{B}$ and thus that $h_m \sim \int \mathbf{B}^2 \mathrm{d}V = E_m$, the helicity goes with the magnetic energy. Because of this it is interesting to talk about the normalised helicity: $\frac{h_m}{E_m}$. The normalised helicity is still dependent on the structure of the magnetic field. Because of this, h_m depends on the values n_t and n_p of the field. The normalised helicity over all space goes with:

$$\frac{h_m}{E_m} \sim \frac{1}{n_t + n_p}. \tag{3.14}$$

Since the magnetic field of these knots goes to zero when $r \to \infty$, the helicity is gauge invariant.

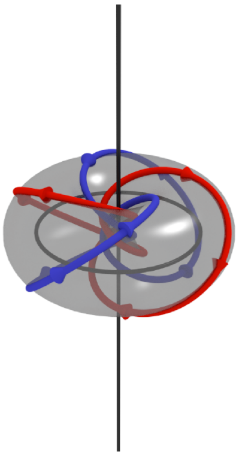

__Figure 3.2:__ The core field lines (red, blue) of a (3,2) knot lying around drawn in torus.

To compare the helicity of two different fields, it is often better to use the normalised helicity $\frac{h_m}{E_m}$ over the helicity h_m since the normalised helicity does not depend on the magnetic field strength. This is very relevant, since the magnetic field strength of a electromagnetic field usually declines over time due to the resistive decay of magnetic energy. The normalised helicity allows us to compare the structure of the a field at two different points in time without having to consider this energy loss.

It may seem counter-intuitive that knots with higher winding numbers n_t, n_p have a lower normalised helicity, but it turns out that the field lines trace a path around the torus with a left-handed writhe. This is counteracted by the right-handed twist of the core field lines around these core field lines. So the writhe and twist have opposing handedness and cancel each other. Knots with higher winding numbers thus reduce the total helicity. Since the time evolution of the magnetic field strength is different between two different (n_t, n_p)-knots, we can use the normalised helicity to compare the different fields.

3.2 Theoretical stability Analysis

3.2.1 Stable solitons in ideal MHD

We will analyse the stability of the $(n_t, 1)$-knots like in [23]. We will show why the knots with Bateman constant n_p of equation 3.9 equal to $n_p = 1$ are considered *stable* solitons. Consider the following two quantities: R and B_0. R is the length scale, or size, of the knot, while B_0 is the magnetic field strength at the origin of the knot. In ideal MHD, the magnetic helicity $h_m = \int \mathbf{A} \cdot \mathbf{B} \mathrm{d}V$ and the angular momentum $M = \rho \int \mathbf{r} \times \mathbf{u} \mathrm{d}V$ of the magnetic field are conserved. The energy E of a field is given by $E = \int \frac{\rho u^2}{2} + \frac{B^2}{2} \mathrm{d}V$. Those three quantities all depend on R and B_0. We call the field *stable* if it can not continuously deform into a configuration with a lower energy. Recall from equation 2.19 that we have to set our velocity $\mathbf{u} = \pm \frac{\mathbf{B}}{\sqrt{\rho}}$. We can now calculate the energy E:

$$\begin{aligned} E &= \int \left(\frac{\rho u^2}{2} + \frac{B^2}{2} \right) \mathrm{d}V \\ &= \int B^2 \mathrm{d}V \\ &= 2 n_t \pi^2 B_0^2 R^3 \end{aligned} \tag{3.15}$$

We can also calculate h_m to be equal to:

$$\begin{aligned} h_m &= \int \mathbf{A} \cdot \mathbf{B} \mathrm{d}V \\ &= \frac{2 n_t}{n_t + 1} \pi^2 B_0^2 R^4 \end{aligned} \tag{3.16}$$

And we find from equations 3.15 and 3.16 that

$$E \sim \frac{h_m}{R}$$

The angular momentum is given by

$$\begin{aligned} \mathbf{M} &= \rho \int (\mathbf{r} \times \mathbf{u}) \mathrm{d}V \\ &= \pm \sqrt{\rho} 4 n_t \pi^2 B_0 R^4 \hat{y} \end{aligned} \tag{3.17}$$

Combining equation 3.15, 3.16 and 3.17, we get the equations for R and B_0:

$$R = \left(\frac{|\mathbf{M}|^2}{8\pi^2 n_t (n_t + 1) \rho h_m} \right)^{\frac{1}{4}}$$
$$B_0 = 2n_t(n_t + 1)\sqrt{\rho} \frac{h_m}{|M|}$$

In ideal MHD, the values for $|M|$ and h_m are conserved over time. Because of this, both R and B_0 are also fixed for all time t. The conservation of h_m prohibits the field to evolve in any way that changes the structure of the field lines, while the conservation of M prohibits the 'spreading' of the field line structure [23].

For $n_p > 1$, the angular momentum $\mathbf{M} = \mathbf{0}$. The disappearance of the angular momentum is realised since the angular momentum of the different families is nullify each other. The above argument for stability depends on the non-zero angular momentum and cannot be used in this case.

3.3 Full MHD simulations

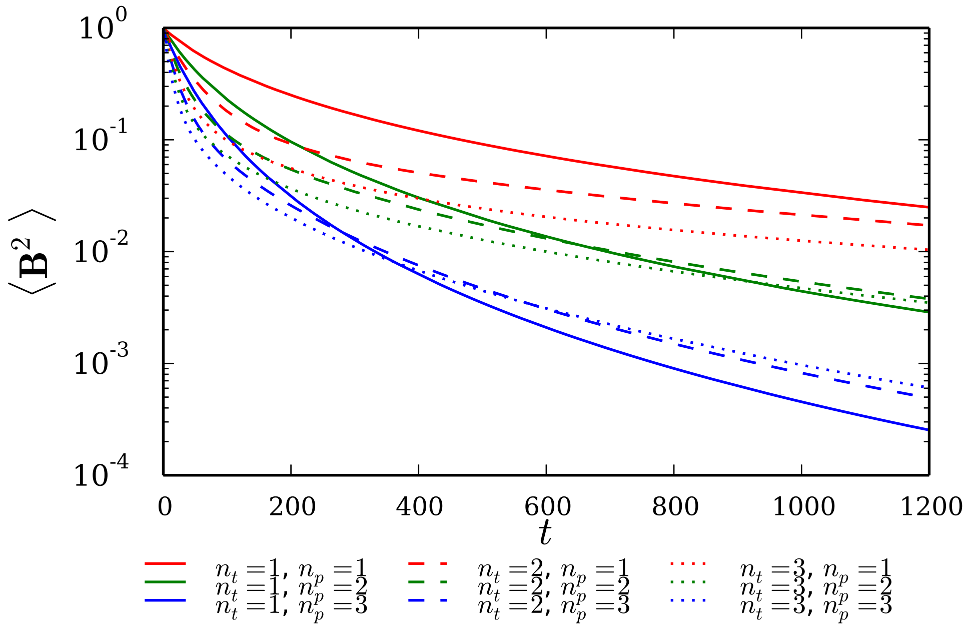

Figure 3.3: *Time evolution of the magnetic energy of different (n_t, n_p)-knots. The magnetic field strength goes down for higher values of t. The speed with which this happens is depends on both n_p and n_t for $t < t_1$ but is later dominated by n_t.*

Version of June 26, 2018– Created June 26, 2018 - 13:50

We simulated nine different fields with different Kedia knots. We looked at all the different pairs (n_t, n_p) with both $n_t \leq 3$ and $n_p \leq 3$. In contrast to ideal MHD simulations, these simulations allowed for a small resistivity and viscosity. During these simulations, energy is allowed to dissipate. The simulations assume an isothermal gas with periodic boundary conditions. We will later see that the choice for boundary conditions does not have a large impact on the simulation. Since we added a nonzero resistivity term, the field lines are allowed to reconfigure. This 'costs' some magnetic energy of the field and also changes the value of the helicity h_m. In the time evolution of the magnetic fields, we can roughly differentiate between two phases. The first phase, where the field lines reconfigure and the second phase where the field line structure is about constant.

Since the reconfiguration of field lines costs energy, we can see those two phases in the time evolution of the mean magnetic field strength $\mathbf{B}^2$. According to figure 3.3, up until some time t_1, this quantity falls of quickly, while it stabilises for $t > t_1$.

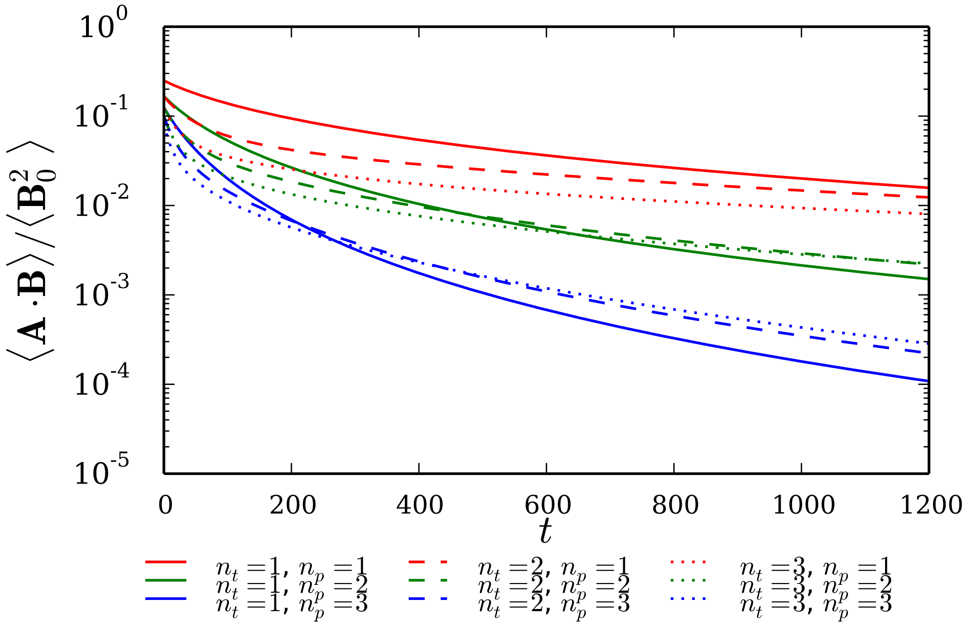

Figure 3.4: *Time evolution of the magnetic helicity of different* (n_t, n_p)*-knots, normalised to the initial magnetic field strength. The helicity goes down for higher values of* t*. The speed with which this happens is dominated by* n_t*.*

Interesting to note is the contribution of both n_t and n_p. For $t < t_1$, we see that the rate of energy loss is higher for higher values of n_t and n_p. In general, the loss of magnetic energy depends on n_p, with higher values of n_p corresponding to a quicker loss of energy. This is in accordance with previous stability analysis, where knots with $n_p = 1$ are stable [23].

Since field lines are allowed to reconfigure in these simulations, the helicity h_m is not conserved. We can see the time evolution of the helicity in figure 3.4. Like the magnetic field strength, the helicity goes down quite fast at the beginning of the simulation before stabilising after some time t.

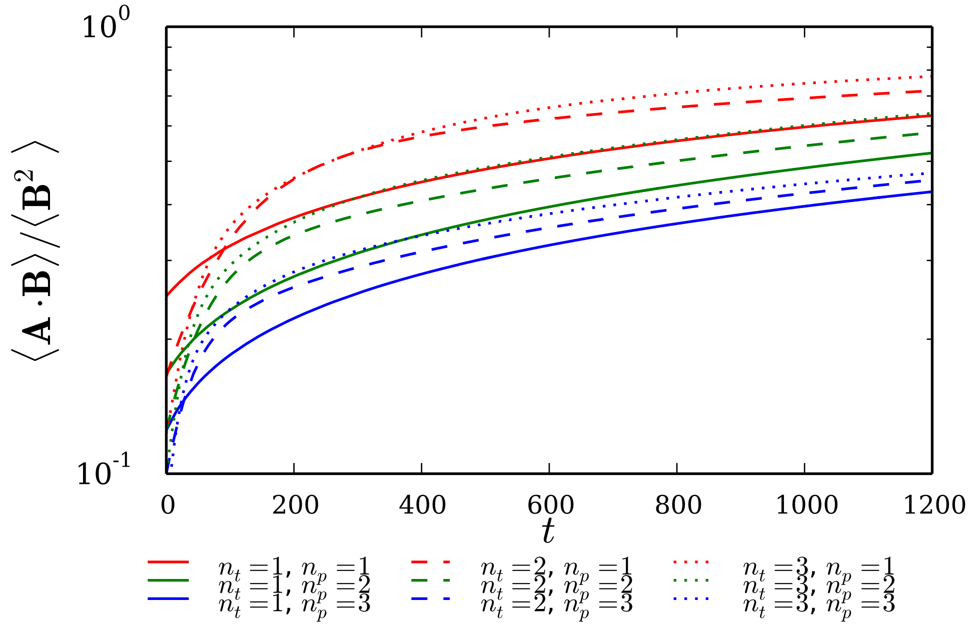

Figure 3.5: *Time evolution of the magnetic helicity of different* (n_t, n_p)*-knots divided by the mean magnetic energy. This quantity seems to stabilise for higher* t*.*

However, the helicity scales with $\mathbf{B}^2$, so it is no surprise that the time evolution of the helicity seems similar to the time evolution of the magnetic field strength. To study to change in the structure of the field lines, it is very informative to look at $\frac{h_m}{E_m}$. As we can see in figure 3.5, this quantity increases relatively quickly during the first few hundred time steps of the simulation. The total increase depends on the value of n_p, slowing down after some time. Since the normalised helicity is only dependent on the configuration of the field lines, this time evolution corresponds with the notion that the structure of the magnetic field changes during the beginning of the simulation, but after a while becomes more stable, only gaining a little normalised helicity due to small deformations.

Another interesting detail of figure 3.4 is that rate of decay of the helicity is lower for knots with the same value for n_t but higher values of n_p. While for shorter time t, the helicity of knots with higher n_p goes down much faster, after a certain time, depending on the value of n_t, the rate of decay of the higher n_p

knots slows down enough that knots with the same n_t, eventually end up with lower helicity. This can be seen very clearly for $n_t = 2$ and $n_t = 3$, but one can also extrapolate from the curves of the helicity of the $n_t = 1$ knots that the $(1,1)$-knot will lose helicity faster than the $(1,3)$-knot.

3.3.1 Robustness of simulation results

Dependence on Boundary Conditions

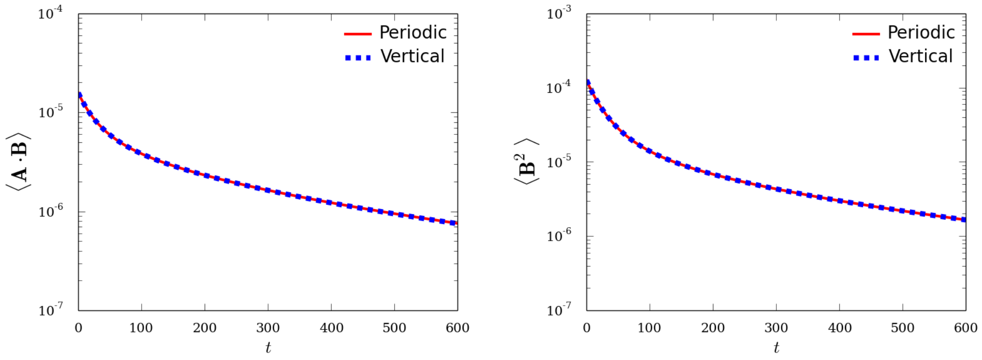

(a) *helicity* ***(b)*** *magnetic field strength*

Figure 3.6: *Time evolution of the helicity and magnetic field strength of the* $(1,2)$*-knot where the initial magnetic field has been scaled with a factor* λ *of* 1 *and* $\frac{1}{2}$.

To show that the choice of the boundary conditions does not make a big difference in our simulations, we simulated the $(2,2)$-knot with both periodic and vertical boundary conditions. In figure 3.6, the helicity and average magnetic field strength of both simulations is plotted. As we can see, the choice of the boundary condition makes almost no impact on the time evolution of the helicity or magnetic strength of the electromagnetic field. This is an indication that the magnetic field is sufficiently small at the borders of our simulation to not see any significant boundary effects.

Dependence on Initial Magnetic Field Strength

Calculating the strength of the initial magnetic field from equation 3.4 gives us different values of the magnetic field strength for the different initial value's of n_p and n_t. In order to effectively compare two different simulations, we scaled the initial magnetic field in such a way that the total energy strength was equal in all simulations. Ideally, scaling the initial magnetic field by a factor λ should not change the outcome of the simulations up to this factor λ. Of course, the

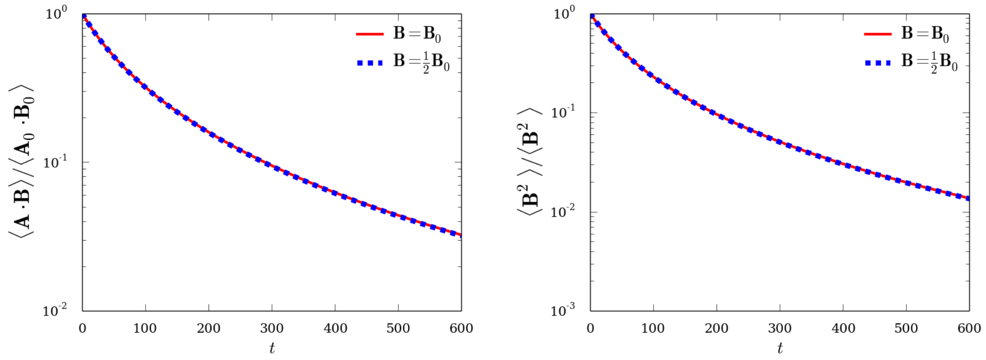

***(a)** helicity*

***(b)** magnetic field strength*

***Figure 3.7:** Time evolution of the normalised helicity and magnetic field strength of the* $(2,2)$*-knot for different boundary conditions.*

initial magnetic field strength could influence the time evolution of the magnetic field. To test the possibility of such an influence, we simulated the same field twice with different magnetic energies, with a difference of a factor 2. This in in the order of the differences of the mean magnetic field of the different initial conditions. The time evolution of the helicity and the magnetic field strength are shown in figure 3.7. As we can see, there is no noticeable difference between the time evolution of the two simulations once normalised. Both the helicity as the mean magnetic strength fall of at the same relative speed. We can also infer this from the governing equations 2.24 and 2.28. When we scale $\mathbf{B}$ with a factor λ, ρ scales with a factor λ^2, and it is clear that both equations are invariant when $\mathbf{B} \rightarrow \lambda\mathbf{B}$.

Dependence on Viscosity

We also tested the impact of the viscosity ν on the time evolutions in the simulation. As stated in 2.3.2, the viscosity used in these simulations is set to $2 \cdot 10^{-4}$. We lowered ν to be $\nu = 10^{-4}$ for one simulation to check for differences in the time evolution. This gives us a Prandtl number of $\frac{1}{2}$. In contrast to the initial magnetic field $\mathbf{B}_0$, changing the viscosity with a factor 2 does influence the outcomes of the simulation. As we can see in figure , especially the helicity is influenced by the viscosity. This means that the structure of the magnetic field lines rearranges quicker when the viscosity is lower. Since liquids with lower viscosity is less resistant to deformation and the magnetic field lines are frozen in the liquid a quicker rearrangement, which adheres to lowering the helicity, is to be expected.

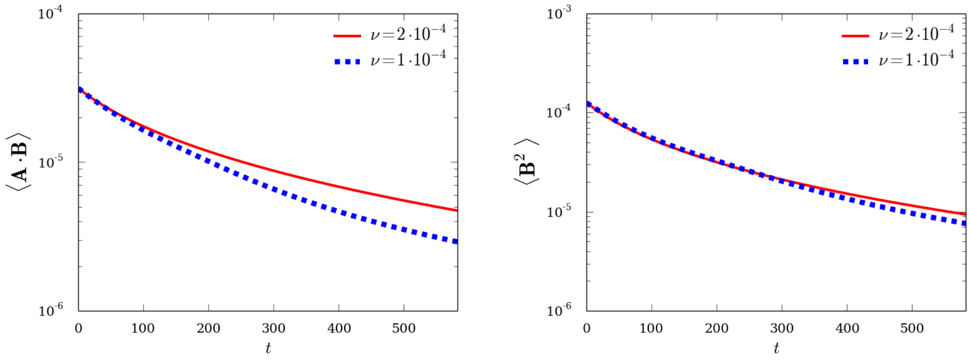

(a) *helicity* ***(b)*** *magnetic field strength*

Figure 3.8: *Time evolution of the helicity and magnetic field strength of the* $(1,1)$*-knot for different values for viscosity.*

Chapter 4

New Magnetic Topologies

In ideal MHD, the topology of electromagnetic fields is protected as we saw in chapter 2.1.2 because the helicity h_m is a constant of motion. While the magnetic field may change over time, the general structure of the field lines, the way they way the may twist and knot around each other, is constrained. In full MHD simulations, where viscous and resistive forces are introduced, h_m is no longer constant. This results in fields whose topology dramatically change over time. In chapter 3 we saw that the helicity of the (n_t, n_p)-knots decreases quite rapidly during the first 200 time steps of the simulations. In this chapter, we will study these new topologies and the effect of the winding numbers on the new topologies of the magnetic field.

4.1 New Magnetic Structures

We saw in section 3.1.1 that at $t = 0$, the **B**-field consists of a few *core field lines*, while the other field lines form surfaces around these core field lines filling space, each core field line the center of a family of nested surfaces. After running numerical simulations on the time evolution of these magnetic fields, we are able to visualise the magnetic fields after arbitrary time t by tracing single field lines. This allows us to study the structure of the new magnetic field. We studied the magnetic structure of different (n_t, n_p)-knots at different times t. We found that the original knot structure is preserved for the whole duration of the simulation for $n_p > 1$. Remember that at $t = 0$, the families of surfaces lying around their respective core field lines fill all of space. However, where two families meet, the z-component of the magnetic field lines is opposite. Here we see that field lines reconnect and form new magnetic surfaces.

The topology of these new structures is dependent on the amount of holes in

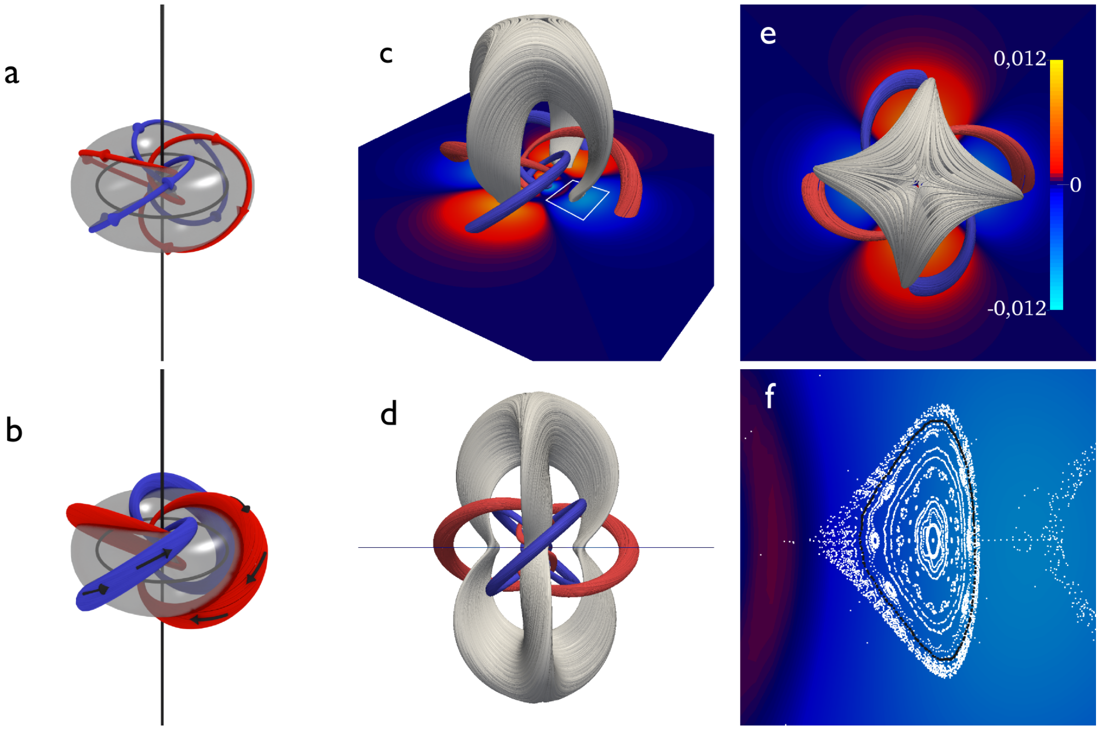

Figure 4.1: *Magnetic surfaces of the* $(3,2)$*-knot after 0 (a,b) and 100 time steps (c-f). We can see the core magnetic field lines of the knot at* $t = 0$ *as a torus knot (a). These core field lines are nested in magnetic surfaces, each formed by a single magnetic field line. The arrows give the direction of the magnetic field (b). The new magnetic surface (white) at* $t = 100$ *is shown from an angled (c), side (d) and top view (d). The colouring of the* $z = 0$ *plane in (c) and (e) corresponds to the* z *component of the magnetic field. The white square in (c) is seen in (f), where a Poincaré plot of the magnetic structure is shown, the white surface of (c-e) is shown in black. (f) shows different surfaces, as well as some magnetic islands.*

it's surface, which we call it's genus g, so the genus of all initial structures is 1. The genus of the new structures dependent on n_p and is given by $g = 2n_p - 1$. Closely related to the genus is the Euler Characteristic $\chi = 2 - 2g$. According to the Poincaré-Hopf index theorem, the Euler characteristic is equal to the sum of the indices of the zero points of the vector field on a surface and we will discuss it further in section 4.2.

In figure 4.1 we see the initial and new structures of the $(3,2)$-knot. Like the initial structures, the new structure also consists of a family of nested surfaces as we can see in figure 4.1 (f). Notice that we also see the formation of magnetic islands, as expected from literature [24, 25]. These will be discussed in section 4.3.

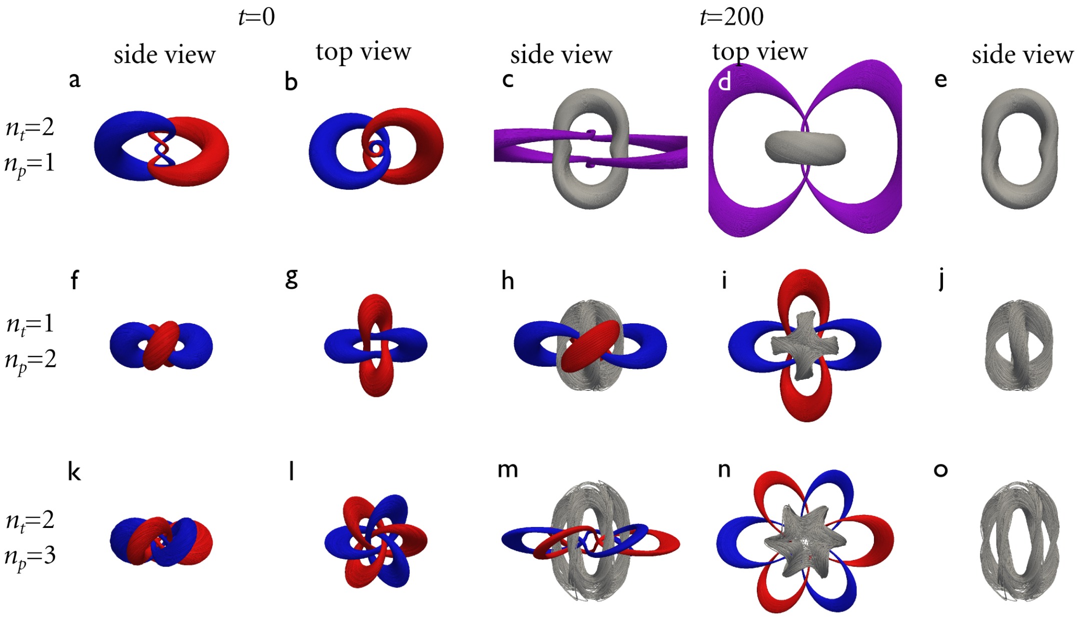

Figure 4.2: *The initial and new magnetic surfaces of the original and new magnetic families. The rows correspond to three different knots, the columns are views at different simulation times. The first two columns picture a side and top view of the initial magnetic surfaces at* $t = 0$ *in red and blue. The next two columns picture the same view at time* $t = 200$*, when a new family of surfaces emerged in grey. The last column pictures only this new magnetic surface. The magnetic surfaces of the* $(2, 1)$*-knot of the first row recombine in the purple form in figure (d) and (e).*

We have simulated all nine (n_t, n_p)-knots with both n_t and n_p smaller then 4. In all simulations, the new structures as described above, appear. If $n_p = 1$, this is a toroidal structure, and $g = 1$. We can see this new surface in grey in figure 4.2 (c-e). While we stated that in general the original structure is preserved, this is not the case for the $(2, 1)$ knot. As we see in the upper row of figure 4.2, the original red and blue families merge into a single new family, pictured in purple. In the case that $n_p = 2$, we observe a new structure that is topologically equal to the triple torus, with genus $g = 3$. This is pictured in figure 4.2 (h-j). For simulations of $(n_t, 3)$-knots, the new surface is topologically equivalent to the quintuple torus (genus $g = 5$) as shown in figure 4.2 (m-o). The new surfaces are shown together with their relative positions to the original magnetic surface families. In general, these surfaces have genus $g = 2n_p - 1$ and they consist of $2n_p$ 'legs' that running parallel to the z-axis. These legs meet on the z-axis, once above and once below the $z = 0$ plane.

The z component of the magnetic field in the new figures is depend on the leg. It is opposite in neighbouring legs, if the magnetic field is pointed in the positive z direction in one leg it is pointed in the negative direction for the legs closest to it. Figure 4.3 shows us the 3 torus where the arrows show the direction of the magnetic field.

The observation that the new magnetic structure is dependent on the choice of n_p, corresponds to our findings in chapter 3. We saw in 3.1.1 that the time evolution of the helicity is largely dependent on n_p.

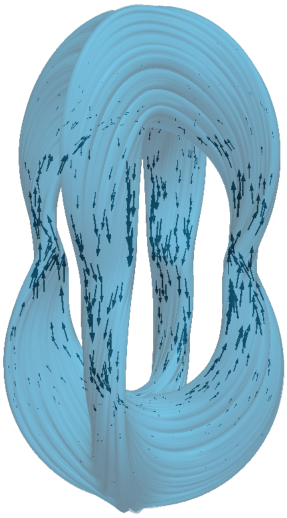

Figure 4.3: *A surface of the three torus in a* $(2,2)$*-knot at time* $t = 50$*. The black arrows show the direction of the magnetic field and are scaled with magnitude.*

4.2 Zero Lines

The chosen factors of α and β in Bateman's construction of $\mathbf{B}$ allow for *zero lines* in our magnetic field. The existence of these lines is dependent on n_p and n_t. Expanding equation 3.4 to

$$\begin{aligned}\mathbf{B} &= \mathrm{Im}\left[\nabla\alpha^{n_t} \times \nabla\beta^{n_p}\right] && (4.1)\\ &= \mathrm{Im}\left[\left(n_t\alpha^{n_t-1}n_p\beta^{n_p-1}\right)\nabla\alpha \times \nabla\beta\right] && (4.2)\end{aligned}$$

shows us that, then $\mathbf{B}$ is zero where α is zero if $n_t > 1$ and where β is zero if $n_p > 1$. α vanishes at the circle of radius r at the z-axis, the set $\{(x,y,z)|z = 0, x^2 + y^2 = r\}$. β vanishes on the $z - axis$, the set $\{(x,y,z)|x = 0, y = 0\}$. During the time evolution of the magnetic fields, the first of these two zero lines, the circle, disappears after some time by contracting to the origin as we can see in figure 4.4. The second, on the z-axis, seems to stay, which explains why the new-formed structures only depend on n_p and why n_t is only relevant for smaller t.

The zero line along the z-axis is essential for the formation of the new magnetic structures. The Poincaré-Hopf index theorem tells us that on a compact differentiable manifold, the sum of the indices of the zeroes is equal to it's Euler characteristic χ. For $n_p = 0$, the new structure is a torus with $\chi = 0$, which allows for a surface vector field without any zeroes. This corresponds with our finding that the z-axis is not a zero line in this case. For the triple and quintuple torus, with Euler characteristic -4 or -8, these zeroes are located where the

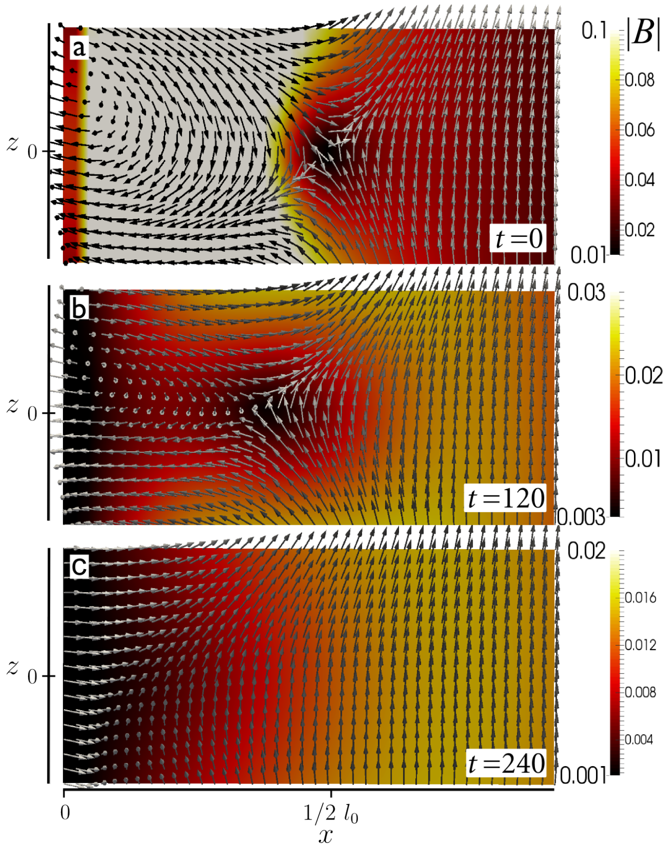

Figure 4.4: *A cut through the xz plane at time $t = 0$(a), $t = 120$(b) and $t = 240$(c). We can see how the null line contracts to the z axis and disappears*

surfaces are intersected by the z-axis, at four distinct points. The index of these zero points is respectively -1 or -2 for $n_p = 2$ and $n_p = 3$, making this zero line a necessary condition for the existence of the new surfaces.

This zero line arises due to the local plasma configuration, and a perturbation of the magnetic field in the z-direction could lift the zero line. Since the new structures are dependent on this zero line, they would not be able to exist if such an external field would remove it. Due to the symmetry of the initial conditions, this zero line is stable under internal perturbations. However, the zero line is not necessarily stable under an external perturbation $\epsilon \mathbf{B}_z$, which could happen in the chaotic magnetic fields of astrophysical objects.

Null points are an important concept in MHD for their role in reconnecting field lines. We find that if in stationary solutions, $\nabla P = \mathbf{J} \times \mathbf{B}$, so the pressure gradient on a zero point disappears. If we consider a compressible plasma, it is found that the Lorentz forces acting within a current sheet are no longer counteracted by this pressure gradient, giving the possibility of a collapse of the magnetic field [26]. This collapse then results in a new current layer around the zero [27]. However, this collapse and restructuring is not always physically feasible [28].

4.3 Magnetic Islands

For each family of surfaces, it is possible for *magnetic islands* to form between two surfaces. These islands are new families of magnetic surfaces and are described in previous literature [24, 25]. The rational transform is is the total rotation of a field line around the corresponding core field line when it has followed this core field line for one loop. We will first consider the islands forming around toroidal surfaces, the surfaces with $g = 1$. These islands form when a field line close to a rational surface is pertubated. Rational surfaces are the surfaces with a rational rotational transform.

An interesting visualisation of these islands, other then by tracing field lines, is done by making a *Poincaré plot*. In these plots, field lines are followed for a certain length, and every time the field line crosses a predefined plane, such as the xy-plane, the location of the crossing is marked. Poincaré plots give a part of the cross section of the magnetic structures and are especially useful to study the form of magnetic islands. In figure 4.5 we see a cutout of a Poincaré plot of the $(1, 2)$-knot at $t = 100$. Here a few magnetic field lines are randomly chosen and every time they cross the xy-plane a point is placed. We can very clearly see magnetic islands. One family of magnetic islands is indicated by black arrows.

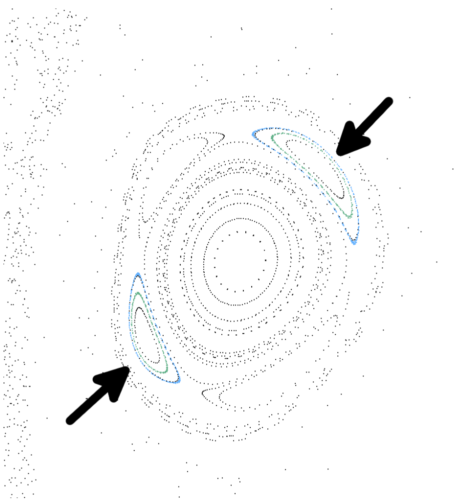

Figure 4.5: *A Poincaré plot of the* $(1, 2)$*-knot at* $t = 100$*. The points in different colours correspond to two distinct surfaces in the same island family. The plot is around the intersection of one of the core field lines with the* $z = 0$ *plane. One family of magnetic islands is marked by two arrows. The colored points correspond to the magnetic islands pictured in figure 4.6*

In figure 4.6 we can see what these islands look like and how they are nested in both each other and their corresponding magnetic structure. Just like the original knots, magnetic islands consist their own families with core magnetic field lines surrounded by nested magnetic surfaces. These island families themselves are fit between two magnetic surfaces of the initial magnetic structure. The magnetic islands wind around the core field

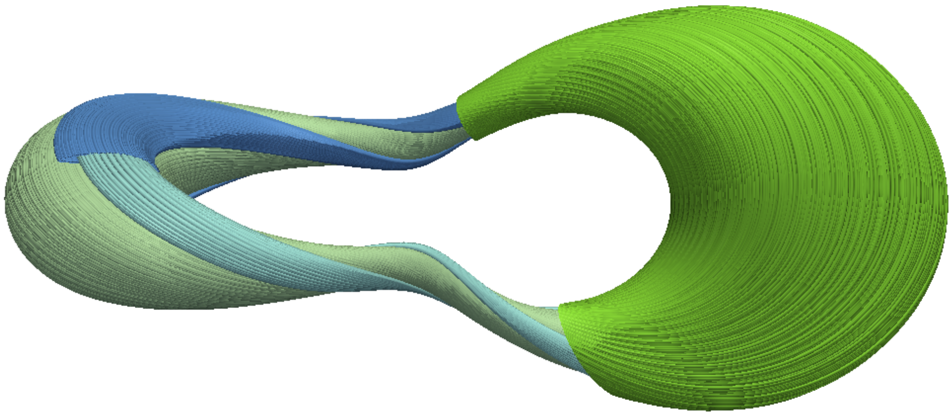

Figure 4.6: *Magnetic islands of the* $(1,2)$*-knot, associated to one of the original structures at* $t = 100$*. Depicted are two nested surfaces of the original family (green), as well as two nested surfaces belonging to one of the magnetic islands (blue). The islands correspond to the points of the same color in figure 4.5*

lines of the initial structure.

4.3.1 Magnetic Islands From Surfaces With Non-trivial Genus

The new magnetic structures discussed in section 4.1 also form magnetic islands. Because of the form of these structures, we can not determine rational surfaces. In fact, the core field line of the structure actually splits up at $z = 0$, and the whole notion of n_t and n_p does not exist. Nevertheless, the Poincaré plots of these new structures show identical features as seen in structures of surfuces of genus 1. This indicates that structures where the surfaces have $g < 1$ also split surfaces into magnetic islands. The corresponding magnetic islands have a very chaotic look but the poincaré plot shows their structure. In figure 4.7 we see a Poincaré plot of the $(2,2)$-knot at time $t = 100$. It is created by seeding 100 random points of magnetic field and following the magnetic field lines through these points for some length. Not only can we see the four legs of the 3 torus crossing the xy-plane, but there is also a plethora of magnetic islands to be found. Every non-white coloured point corresponds with one island structure,

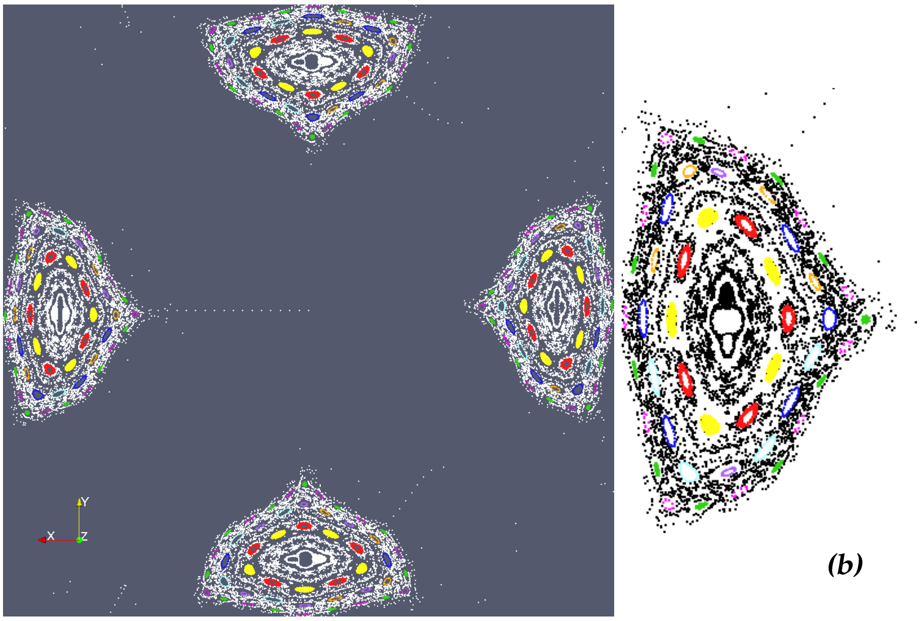

(b)

(a)

Figure 4.7: *(a) Poincaré plot of the* $(2, 2)$*-knot at* $t = 100$ *through the* $z = 0$ *plane. Different islands are marked in different colours.* $t = 100$*. (b) cutout of the figure in (a) to show more detail.*

which is again a family of magnetic surfaces with one core field line.

Again, we can see that these islands lie in between the magnetic surfaces of these new magnetic structures. These islands consist own nested magnetic surface families with a core field line. An example of two of those field lines is given in figure 4.8a.

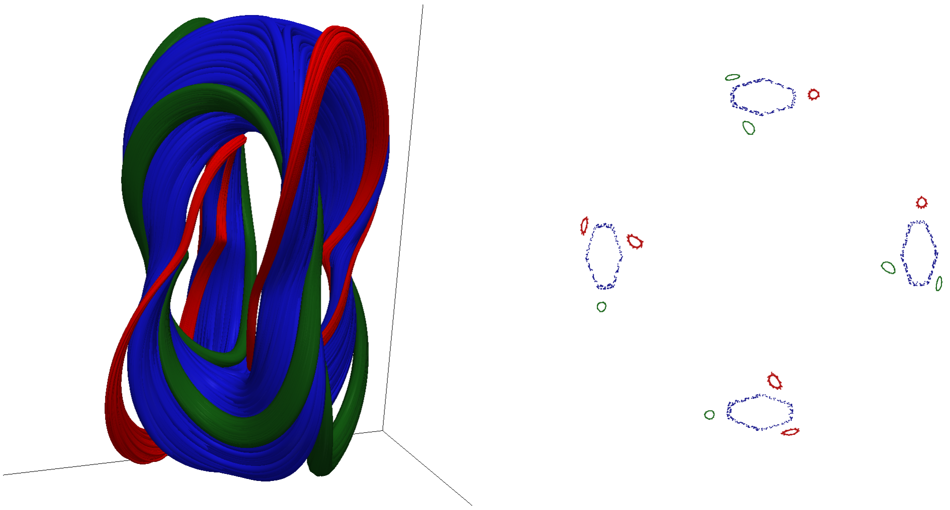

(a) **(b)**

Figure 4.8: *(a) Two islands (red, green) lying around the 3 torus of a* $(2,2)$*-knot (blue) at* $t = 50$ *and (b) The Poincaré plot of this three surfaces in the* xy*-plane.*

Chapter 5

Conclusion

In ideal MHD helicity is a constant of motion, fixing the topological structure of magnetic fields. The ideal MHD equations allow for stable and stationary plasma configurations. We generated several topological non-trivial magnetic fields using Kedia's construction. These fields have a non-zero helicity and consist of several linked families of nested magnetic surfaces around core field lines filling all of space. These fields form stationary solutions in ideal MHD. These fields are parameterised by their toroidal and poloidal winding numbers n_t and n_p. We modified the ideal MHD equations to include the effect of both resistive and viscous forces. We numerically analysed the time dependent behaviour of several (n_t, n_p) fields in resistive MHD using the PENCIL code. Helicity is not conserved in resistive MHD and thus allows for changes in the magnetic field topology over time.

In most cases, the initial magnetic structures of these magnetic fields persists during the whole simulation. The few times they did not, we observed that the core field lines reconnected and fused together. However, after some time these structures did not fill up all of space anymore and we also saw new structures emerge on the border of the two different families of initial structures. These new structure have an Euler Characteristic depending on the value of n_p in the initial magnetic field. For $n_p > 1$, the Euler Characteristic is non-zero. A surface with a non-zero Euler Characteristic has to have zero points and these zero points are realised by a zero line along the z-axis. Intersection of the new surfaces and the z-axis allows for zero points on these new structures. Since the new structures are dependent on n_p, the magnetic field strength and helicity are largely dependent on n_p too, especially after some time t when the topological structure of the magnetic field does not change significantly anymore. The value of n_t also influences the loss of magnetic energy and helicity, especially at low t, but the zero line it induces, a circle around the z-axis, contracts and disappears in contrast to the zero at the z-axis. In both the initial structures as the new ones, we notice families of magnetic islands. The magnetic islands on the structures with Euler Characteristic zero has are predicted in literature and form close to rational surfaces. The concept of rational surfaces does not generalise to surfaces with a non-zero Euler Characteristic, but the splitting of surfaces into magnetic islands did occur their as well.

The dependence of the new magnetic structures on the zero line along the z-axis makes it that these structures are very sensitive to external magnetic fields and we do not expect them to emerge in astrophysical plasma's. However, it is possible to create such zero lines on the meeting border of two opposing magnetic fields.

Further research on this subject could include analysing fields with higher n_t and n_p, or increase the time scales of he simulations that have been done. One could also study the effect of the viscosity and resistivity on the old and new structures or generalise the simulations by allowing temperature gradients.

Appendix A

Article: Magnetic Surface Topology in Decaying Plasma Knots

The simulations and analysis presented in this thesis have resulted in a publication in the New Journal of Physics on February 23rd 2017 [29]. The article has integrally been added in this appendix.

Magnetic Surface Topology in Decaying Plasma Knots

C. B. Smiet[1], **A. Thompson**[2], **P. Bouwmeester**[1], **and D. Bouwmeester** [1,2]

[1]Huygens-Kamerlingh Onnes Laboratory, Leiden University, P.O. box 9504, 2300 RA Leiden, The Netherlands
[2]Department of Physics, University of California Santa Barbara, Santa Barbara, California, 93106, USA

Abstract. Torus-knot solitons have recently been formulated as solutions to the ideal incompressible magnetohydrodynamics (MHD) equations. We investigate numerically how these fields evolve in resistive, compressible, and viscous MHD. We find that certain decaying plasma torus knots exhibit magnetic surfaces that are topologically distinct from a torus. The evolution is predominantly determined by a persistent zero line in the field present when the poloidal winding number $n_p \neq 1$. Dependence on the toroidal winding number n_t is less pronounced as the zero line induced is contractible and disappears. The persistent zero line intersects the new magnetic surfaces such that, through the Hopf-Poincaré index theorem, the sum of zeroes on the new surfaces equals their (in general non-zero) Euler characteristic. Furthermore we observe the formation of magnetic islands between the surfaces. These novel persistent magnetic structures are of interest for plasma confinement, soliton dynamics and the study of dynamical systems in general.

PACS numbers: 52.65.-y,52.35.Vd, 52.65.Kj,52.30.-q

Submitted to: *New J. Phys.*
Keywords: Magnetic reconnection, magnetic topology, magnetic helicity, topological solitons

It is remarkable how abstract topological concepts are directly relevant to many branches of science. A prime example is the Hopf map [1], a non-trivial topological structure that has found applications in liquid crystals [2], molecular biology [3], superconductors [4], superfluids [5], Bose-Einstein condensates [6, 7], ferromagnets [8], optics [9, 10, 11], and plasma physics [12, 13]. This article deals with topological aspects of novel persistent plasma configurations that emerge from decaying plasma torus knots.

Due to the generally high electrical conductivity of plasma described by Magnetohydrodynamics (MHD), large electrical currents can flow and plasmas are heavily influenced by the resulting magnetic forces. The zero-divergence magnetic fields can lead to closed magnetic field lines, field lines that ergodically fill a magnetic surface, and field lines that chaotically fill a region of space. In ideal (zero-resistance) MHD the magnetic flux through a perfect conducting fluid element cannot change, leading to frozen in magnetic fields in the plasma [14]. This implies that in ideal MHD magnetic topology and magnetic helicity is conserved [15, 16, 17].

In 1982 Kamchatnov described an intrinsically stable plasma configuration [13] with a magnetic topology based on fibers of the Hopf map [18]. This type of MHD equilibrium, where the fluid velocity is parallel to the field and equal to the local Alfvén speed, was shown by Chandrasekhar to be stable [19], even in specific cases in the presence of dissipative forces [20]. Quasi stable self-organizing magnetic fields with similar magnetic topology to Kamchatnov's field (but different flow) have recently been demonstrated to occur in full-MHD simulations [12]. Here the final configuration is not a Taylor state, which is consistent with recent findings in [21].

Recently the class of topologically non-trivial solutions to Maxwell's equations has been extended by including torus knotted fields [22]. Another way of obtaining such solutions, for massless fields of various spins, is to use twistor theory [23]. The magnetic fields of the $t = 0$ solutions in [22], have been used to construct novel plasma torus knots [24], solutions to the ideal incompressible MHD equations.

To investigate the potential importance of plasma torus knots for realistic plasma the influence of dissipation has to be investigated. Dissipation can lead to breaking and reconnection of field lines and thereby change the magnetic topology. In this letter we show numerically that novel persistent magnetic structures emerge that are characterized by a non-zero Euler characteristic. Through the Poincareé Hopf index theorem this leads to precise statements about zeroes in the magnetic fields which further clarifies the plasma structures. Furthermore magnetic islands are observed in between the new magnetic surfaces.

1. Plasma torus knots

An ideal MHD soliton, as defined in [13, 24], is a static configuration of magnetic field $\boldsymbol{B}$, fluid velocity $\boldsymbol{u}$, and pressure p that satisfies the ideal, incompressible MHD equations. The fluid field and pressure that solve this can be inferred from the momentum equation, which can be written as:

$$\frac{\partial \boldsymbol{u}}{\partial t} + \boldsymbol{u} \cdot \nabla \boldsymbol{u} - \frac{1}{\rho} \boldsymbol{B} \cdot \nabla \boldsymbol{B} + \frac{1}{\rho} \nabla \left(p + \frac{B^2}{2} \right) = 0, \tag{1}$$

and the induction equation:

$$\frac{\partial \boldsymbol{B}}{\partial t} = \nabla \times (\boldsymbol{u} \times \boldsymbol{B}) \,. \tag{2}$$

In the ideal and incompressible case the fluid field and pressure corresponding to the soliton are given by

$$\boldsymbol{u} = \pm \frac{\boldsymbol{B}}{\sqrt{\rho}}, \quad p = p_\infty - \frac{B^2}{2}, \tag{3}$$

respectively. Already in 1956 in a paper titled "On the stability of the simplest solution of the Equations of Hydromagnetics", Chandrasekhar noted that this represents an *exact stationary solution* and proved it to be stable against linear perturbations.

Kamchatnov analyzed this solution for the specific case where the magnetic field and velocity field are given by the Hopf map, every single field line is linked with every other. The static magnetic field of the Kamchatnov-Hopf soliton, whose magnetic field is identical to the $t = 0$ magnetic field of an electromagnetic solution in free space [9] can be obtained in various ways. Bateman's construction [25] of describing a (null) electromagnetic field via two Euler potentials α and β such that $\boldsymbol{F} = \boldsymbol{E} + i\boldsymbol{B} = \nabla\alpha \times \nabla\beta$, is well suited to generate new solutions to Maxwells equations with torus knotted field lines [22]. The class of torus knot solitons, of which the Kamchatnov-Hopf soliton is an element, are the solutions to the ideal MHD equations where the velocity and fluid field are identical to the magnetic field of these EM solutions [24].

The torus knot solitons are constructed using the following complex-valued Euler potentials

$$\alpha = \frac{r^2 - 1 + 2iz}{r^2 + 1}, \text{ and } \beta = \frac{2(x - iy)}{r^2 + 1}, \tag{4}$$

followed by a substitution $r \to r/r_0$ (where $r^2 = x^2 + y^2 + z^2$) to rescale the configuration. Taking $\mathrm{Im}\left[\nabla\alpha \times \nabla\beta\right]$ gives the magnetic field of the Kamchatnov-Hopf soliton. Generalizing this construction by raising α to a positive integer power n_t which we call the toroidal integer, and β to a positive integer power n_p which we call the poloidal integer, the magnetic field of a (n_t, n_p) plasma torus knot is obtained via:

$$\boldsymbol{B} = \frac{c \ \mathrm{Im}[\nabla\alpha^{\mathrm{n_t}} \times \nabla\beta^{\mathrm{n_p}}]}{\sqrt{a}}. \tag{5}$$

Where c is a scaling constant with correct dimensions and $a = \int \left(\mathrm{Im}[\nabla\alpha^{\mathrm{n_t}} \times \nabla\beta^{\mathrm{n_p}}]\right)^2 \mathrm{d}^3x$, integrated over all space, is a normalization factor that provides all magnetic field configurations with the same magnetic energy.

As noted, the plasma (1,1) torus knot is the Kamchatnov-Hopf soliton: every magnetic field line is a circle that is linked with every other field line. Otherwise the field configuration is characterized by a finite set of core field lines that each form an (n_t, n_p) torus knot and around which other field lines span nested magnetic surfaces

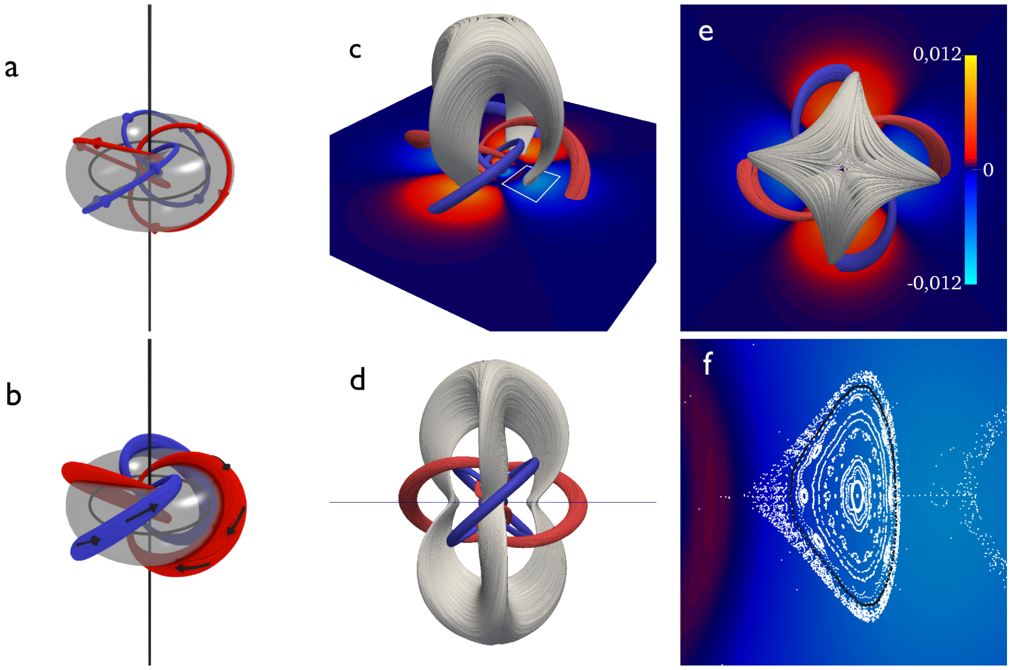

Figure 1. New magnetic surfaces and their relation to the structure in the initial $n_t = 3$ and $n_p = 2$ plasma torus knot. The original plasma torus knot structure consists of two core field lines that form $(3, 2)$ torus knots (a). Other field lines form magnetic surfaces around one of the two core field lines, as shown in (b). The black lines indicate the zero lines in the field. The new magnetic surface forms between the two core field lines, as shown from angled view (c), side view (d) and top view (e). Magnetic surfaces with the field line topology of the original field are shown in red and blue, the new surface in grey. The plane at $z = 0$ shows the z-component of the magnetic field (scale bar given in panel (e)). (f) Poincaré plot of the magnetic structure inside the non-toroidal surfaces, showing nested surfaces, as well as magnetic islands. The white square in panel (c) indicates the size of the region in panel (f).

[22, 24]. Figure 1 (a) and (b) show an example of a plasma torus knot magnetic field configuration with toroidal integer $n_t = 3$ and a poloidal integer $n_p = 2$. Figure 1 (a) shows that there are two core field lines that each form a $(3, 2)$ torus knot, and figure 1 (b) shows two magnetic surfaces spanned by field lines close to the two core field lines.

The magnetic helicity, defined as

$$h_m = \int \boldsymbol{A} \cdot \boldsymbol{B} d^3x, \tag{6}$$

(where $\boldsymbol{A}$ is defined through $\boldsymbol{B} = \nabla \times \boldsymbol{A}$) is an invariant of ideal MHD. The total magnetic helicity of the plasma torus knots is found by integrating equation 6 over all space, and is given by

$$h_m = -\frac{r_0}{n_t + n_p}, \tag{7}$$

where we have used $\boldsymbol{A} = c\ \mathrm{Im}[\beta \nabla \alpha]/\sqrt{\mathrm{a}}$. The magnetic field of the torus knots goes to zero at infinity, such that this helicity is gauge invariant. The magnetic helicity is reduced in the plasma torus knots with higher values of n_p and n_t. This reduction is qualitatively understood by noting that the core field lines trace a path around the torus with a left-handed writhe while the magnetic surfaces have a right-handed twist around the core field lines. Since both writhe and twist contribute to the helicity the opposite signs cancel each other [26, 27] and higher values of toroidal and poloidal integers reduce the total magnetic helicity.

The conservation of energy, angular momentum, and magnetic helicity, can provide stability to certain plasma configurations. As shown in [24] only the plasma torus knots with $n_p = 1$ have non-zero angular momentum and are able to form stable configurations in ideal MHD. We now investigate the solutions represented by equations 5 and 3 in the case of a non-ideal plasma by adding compressibility, magnetic diffusivity, and viscosity.

2. New emerging surfaces

We numerically study the dynamics of plasma torus knots using the PENCIL code, a high-order finite difference code for compressible MHD [28, 29]. In resistive MHD the equation 1 gains a viscous term $-\boldsymbol{F}_{\text{visc}}$ and equation 2 gains a resistive term $-\nabla \times \eta(\nabla \times \boldsymbol{B})$. In the compressible case the density ρ is calculated by a continuity equation, and an isothermal equation of state is used such that $p = c_s^2 \rho$. The equations solved and the details of how the resistive terms are implemented are described in Appendix A. The characteristic length is set to $r_0 = 1/2l_0$ and the simulation box size is $(2\pi l_0)^3$ with 256^3 grid points. The viscosity and magnetic diffusivity were set to $\nu = \eta = 2 \times 10^{-4}$, giving a Prandtl number of unity.

We observe a dramatic change in the magnetic topology during a rapid first phase in the dynamics characterized by field lines pinching off and reconnecting. During this reconfiguration new magnetic surfaces are formed which have in general a different topology. After this first phase the new configurations persist in time and have an unchanging magnetic topology and a decreasing field strength due to the finite resistivity. For example Fig. 1 (c), (d), and (e) give an angled view, a side view, and a top view of a new magnetic surface in the (3,2) plasma torus knot.

The magnetic fields close to the center of the initial plasma configuration have strong components in opposite directions along the z axis. The dynamical principle of the formation of the new surfaces is that regions of largest counter propagating fields (here the center of the configuration) will have highest dissipation which pinches off field lines. The remaining part of the field lines will find nearby pinched-off fields lines with whom they connect resulting in the new magnetic surfaces.

An interesting interpretation of the emergence of the observed structures is given by the mechanism of the flow of helicity across scales as demonstrated by Scheeler et al. in [30]. They show that the component of fluid helicity caused by the linking of vorticity filaments in fluids will, through localized reconnections translate to larger scale writhe,

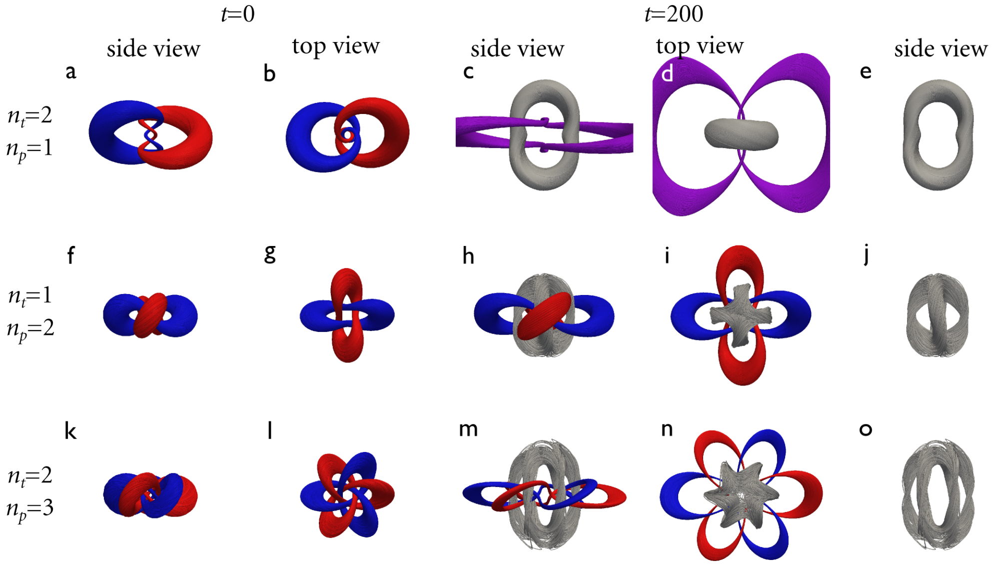

Figure 2. Initial and emerging magnetic surfaces. first column: side view (along x-axis) of magnetic surfaces at $t = 0$. Second column: top view at $t = 0$. Third column: side view at t=200, where both new magnetic surfaces (grey) and the remains of the original magnetic surfaces can be seen. Fourth column: top view at t=200. Fifth column: Only the new magnetic surfaces. The initial magnetic surfaces are colored in red and blue, while magnetic surfaces that were not initially present are colored grey. The magnetic surfaces in figure (a) and (b) can be seen to recombine into the single magnetic surface shown in figure (d) and (e) (purple).

and eventually to twist, present on the largest scale, approximately conserving total helicity. The parallels between fluid and magnetic helicity have been established since their conception [15]. In this interpretation the effect of the localized reconnection at the center of the configuration can be seen as removing the writhing and linking of the initial magnetic surfaces, resulting in a configuration where helicity is present as twist in the antiparallel legs of the new magnetic structure.

The topology of a surface is characterized by its genus g, which is equal to the number of holes in that surface. A torus has only one hole, and therefore genus 1, but the new (grey) emerging surface is a surface with three holes, a triple torus. The genus of a surface is related to the Euler characteristic by $\chi = 2 - 2g$, which is an important topological invariant. The Poincaré-Hopf index theorem relates the Euler characteristic to zero points of a vector field on the surface as we shall show in section 4 and is therefore an important quantity in analyzing the new plasma structures.

The new surface drawn in grey is part of a set of nested surfaces with the same topology. This can be seen from the Poincaré plot in figure 2 (f). Note that there also appear, as expected from references [12, 31], magnetic islands (see the section on islands).

Simulations have been performed for the nine combinations with n_t =1, 2, 3 and n_p =1, 2, 3. Figure 2 shows the results for (n_t, n_p) equal to (2,1), (1,2) and (2,3).

The configurations with $n_p = 1$ all reconfigure in a way such that a new set of toroidal nested surfaces appear. The relation between this new set (shown in grey) and the original two sets can be seen for $n_p = 1$, $n_t = 2$ in figure 2(c)-(e), and is such that the new surfaces are tori lying in the x, z-plane. The original (red and blue) surfaces have merged into the purple surface, and will eventually disappear from the simulation. Most notably however, also here we observe magnetic surfaces that are not topologically a torus, but a triple torus as seen in figure 2 (h)-(j), and a quintuple torus in figure 2 (m)-(o). These new surfaces are shown at simulation time $t = 200$, to illustrate their relationship to the original magnetic surfaces. At later times in the simulation the original surfaces will disappear , and only the surfaces with the new magnetic topology persist.

The created surface depends on n_p directly. When $n_p = 1$ the new surface is a torus, when $n_p = 2$ a triple torus ($g = 3$), and when $n_p = 3$ a surface which has genus $g = 5$. These magnetic surfaces consist of $2n_p$ twisted 'legs' that run parallel to the z-axis. These legs meet on the z-axis above and below the $z = 0$ plane. In half the legs the magnetic field is oriented in the positive z-direction, in the other half in the negative z-direction. Where the legs meet the field exhibits a magnetic cusp geometry and the field lines switch over from one leg to the other.

3. Magnetic Decay

If we look at the time evolution of the mean magnetic energy $\langle \boldsymbol{B}^2 \rangle / \langle \boldsymbol{B}_0^2 \rangle$, shown in figure 3, we see that the configurations with $n_p = 1$ (red curves) show the lowest energy loss, and thus the highest stability, followed by the fields with $n_p = 2$, and finally the fields with $n_p = 3$. The lowest loss of energy for fields where $n_p = 1$ is consistent with the analytical stability analysis in [24] that predicts plasma torus knots with $n_p = 1$ to be stable. Figure 3 (b) shows the evolution of normalized magnetic helicity (magnetic helicity divided by magnetic energy). Because the fields start out normalized by energy, their initial value corresponds with the result of equation 7. The increase in normalized magnetic helicity can be seen as the result of the magnetic energy decaying faster than the helicity.

We observe that during the entire simulation the fluid velocity $\boldsymbol{u}$ remains to a high degree parallel and equal in (dimensionless) magnitude to the magnetic field $\boldsymbol{B}$, even as the magnetic topology changes. The stability of the configuration is predicated on this condition being maintained. Balancing the momentum equation in this way is fundamentally different from the stability exhibited by a solution to the Grad Shafranov equation [32] or a force-free field [14].

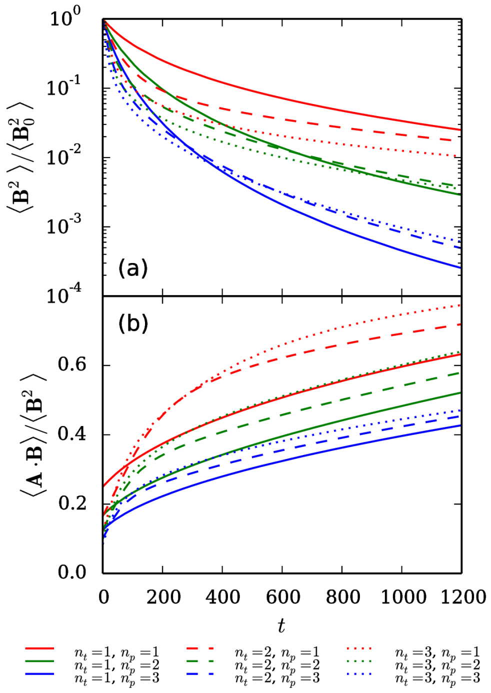

Figure 3. Decay of magnetic energy for all plasma torus knots with n_t and n_p ranging from 1 to 3. (a) Magnetic field strength as a function of time. It is clear that the higher values of n_p decay faster. Initially higher values of n_t decay faster as well, but this trend reverses with sufficient time. (b) Normalized magnetic helicity as a function of time.

4. Zero lines

The initial fields of the plasma torus knots contain nonsingular points where the magnetic field strength vanishes if either n_p or n_t is not unity. This can easily be seen by expanding equation 5 into:

$$\boldsymbol{B} = \frac{c\mathrm{Im}\left[(n_t \alpha^{n_t-1} n_p \beta^{n_p-1})\nabla\alpha \times \nabla\beta\right]}{\sqrt{a}}, \tag{8}$$

which goes to zero at any point where $\alpha = 0$ if n_t is not 1, or where $\beta = 0$ if n_p is not 1. This gives rise to vortex nulls in the field via the method described [33]. For $n_t \neq 1$ the field vanishes on the circle in the $z = 0$ plane $\{(x, y, z)|z = 0,\ x^2 + y^2 = r_0\}$, and for $n_p \neq 1$ the field vanishes along the entire z-axis. The field only approaches zero linearly around the circular null if n_t is two, and similarly for the straight null if $n_p = 2$, otherwise the null is higher-order.

Null points have been described extensively in the literature [34, 35] because of their role in reconnection [36]. We analyze the null lines in the field using the method presented in [35], by constructing the linearization matrix $\mathbf{M}$ whose indices are given

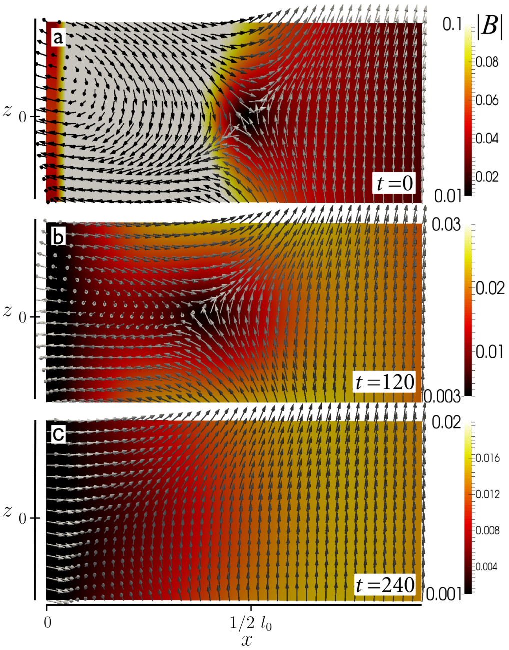

Figure 4. Cut through the x-z plane showing the disappearance of the circular null line. (a) Initial field, (b) field at time $t = 120$, and (c) disappearance of the null line by merging with the straight null on the z-axis at $t = 240$.

by $M_{ij} = \partial_j B_i$, (see Appendix B). The field around a null can be characterized by the three eigenvectors of this matrix [35] that represent the directions from which field lines approach and leave the null. Around the null lines, these three vectors are orthogonal, with the zero-eigenvalue eigenvector in the direction of the null line. The other two vectors determine two orthogonal directions, one from which the magnetic field lines approach the null, and the other determines the direction in which field lines leave the null. These two vectors rotate around the zero line as one moves along the zero line. The number of rotations of these vectors around the straight null is n_t, and the number of rotations around the circular null is n_p (see Appendix B).

The zero circle disappears by contracting to a point on the origin. This process is shown in figure 4, and it explains why the final configuration depends predominantly on the poloidal index n_p, which determines the topology of the new magnetic surfaces.

The Poincaré-Hopf Index Theorem states that the sum of the indices of the zeroes of a vector field on a compact, oriented manifold is equal to the Euler characteristic χ of that manifold. A magnetic surface is such a manifold, and the magnetic field necessarily is a vector field in that surface. A toroidal surface ($\chi = 0$) allows a smooth vector field without any zero points. A magnetic surface can only form the observed triple torus ($\chi = -4$), or quintuple torus ($\chi = -8$) if there are points where the magnetic field is zero, and the indices of these zeroes then must sum to -4 or -8 respectively. These zeroes are provided by the zero line on the z-axis, that intersects them exactly four times and carries index -1 or -2 (where the index is defined by the field restricted to the two-dimensional surface perpendicular to the zero line) if $n_p = 2$ or $n_p = 3$ respectively. Therefore these surfaces can exist by grace of the zero line, and they can only persist if the zero line persists.

It is generally assumed that extended zeroes are unstable [17, 37, 35]. In our simulations however we observe that if the magnetic field starts at zero on the straight null, this zero line persists during entire simulation. This is in contrast to the zero line on the circle in the $z = 0$ plane, which disappears quickly, and is not present in the final configuration, as is shown in figure 4.

The Poincaré Hopf index of a nonsingular zero point can be defined, as for example in [38]. Here it is shown that the vector field on the boundary of a neighbourhood of the nonsingular null can be extended to a field in the interior of that neighbourhood with finitely many singular nulls, and the sum of these indices is defined as the total index of the null. The total sum of the indices of nonsingular nulls is equal to the Euler characteristic of the manifold in which these nulls reside. The Euler characteristic of $\mathbb{R}^3$ is 0, and therefore the indices of the null lines sum to zero. This explains how the zero on the circle can contract to a point, and disappear, leaving no zero point behind, or merge with the null line on the z-axis.

The null on the z-axis does not move, and persists in time. This does not necessarily imply that the zero line is stable, as any external perturbation of the form $\epsilon \boldsymbol{B}_z$ will make the null disappear, but the internal plasma dynamics do not make the null disappear. This persistence can be understood as a consequence of the symmetry of the field around the z-axis. The symmetry of the matrix $\mathbf{M}$ entails that the eigenvectors of $\mathbf{M}$ are orthogonal around the zero line, such that the field approaches the null from two orthogonal directions, in a plane perpendicular to the null line. The restriction of the vector field to this two-dimensional plane has a topological singularity (an X-point), and we observe that no field in the z-direction is created, allowing the zero line to persist, and the non-toroidal surfaces to exist.

5. Magnetic Islands

The new magnetic surfaces are part of a set of nested surfaces with the same topology. There are, similar as what is observed from breaking up of toroidal magnetic surfaces [31, 12], also magnetic islands between these surfaces. Between the non-toroidal magnetic surfaces these islands can take very different, and complicated forms, tracing out intricate knots and links in the space between the intact non-toroidal surfaces (see figure 5).

Magnetic islands are generally described by casting magnetic field line flow in terms of a Hamiltonian dynamical system, and the magnetic surfaces are invariant tori in this system. In the unperturbed system, the field will consist only of nested toroidal surfaces characterized by a rotational transform. A perturbation will cause some tori to break up into island chains. Close to rational surfaces, (surfaces where the rotational transform is

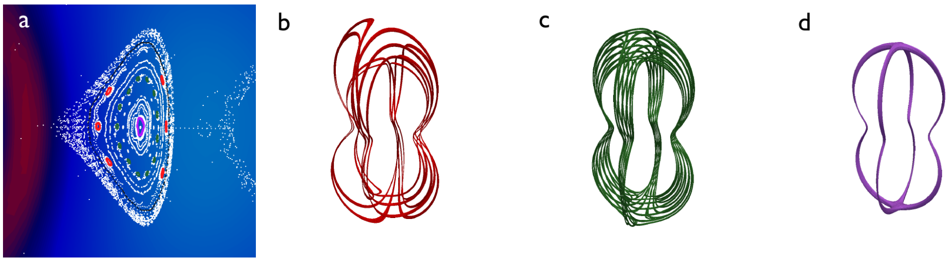

Figure 5. Magnetic surfaces and islands in the region with the new magnetic surfaces. (a) The Poincaré map of the region, indicating where the magnetic islands in (b) (red), (c) (green), and an inner surface with the same topology as the set of islands (d) (purple) are located in the nested set of surfaces.

rational, i.e. field lines form closed curves) field lines will form surfaces that lie around one of the closed field lines of the original rational surface.

The islands in these non-toroidal surfaces also originate from an intact surface, as can be seen in figure 5 (a). The field in the cross section of one upwards oriented 'leg' of the branched surface are rotated, and then split over the two downwards oriented legs, to be split and combined again. Because of this a rotational transform of the surface cannot be defined. Even though every point of the cross section will eventually map back to the cross section, this mapping is not necessarily continuous, and not in general a rotation. We do observe field structures that strongly resemble magnetic islands, but these island chains need not be symmetrically distributed across the surface, as is the case for the structure in figure 5 (b). Because these islands form around a field line lying on a non-toroidal surface, their path need not be a torus knot, but can follow a differently knotted path.

6. Conclusions and Discussion

We have studied a class of plasma torus knots in resistive plasma, which consist of linked and knotted core field lines surrounded by nested toroidal surfaces. n_p has strongest influence on the time evolution of these structures. Large values for n_t slow down the decrease of $\langle \boldsymbol{B}^2 \rangle$ only at high t. These dynamics can be understood by the dynamics of the zero lines, where the circular null, caused by $n_t > 1$ is able to contract to a point and disappear, but the straight null caused by $n_p > 1$ persists, and allows for new magnetic ordering with low energy loss.

In the resistive simulations the magnetic topology is not conserved, and new and interesting magnetic topologies are created. Structures with genus 3 and 5 are observed, and persist in the simulations. These structures also exhibit magnetic island formation, which has a different character to islands that emerge from toroidal magnetic surfaces.

Given the crucial role played by the extended zero in the plasma configuration resulting from initial symmetry, it seems unlikely that magnetic surfaces with non-zero

Euler characteristic occur in the turbulent plasmas encountered in an astrophysical context. It is however possible to engineer this symmetry. A zero line can occur where sets of opposing fields meet, and can be created by sets of opposing coils, as is done in the cusp geometry[39]. These non-toroidal surfaces suggest new topologies for magnetic confinement fusion devices, essentially a marriage of the cusp fusion concept[39] or polywell fusion concept[40] and the stellarator concept[41].

acknowledgments

The authors would like to acknowledge Jan Willem Dalhuisen, Joost Opschoor, Joe Swearngin, Simon Candelaresi, Roland van der Veen, Gunnar Hornig, David Pontin and Keith Moffatt for stimulating discussions and invaluable feedback. This work is supported by NWO VICI 680-47-604, NSF Award PHY-1206118 and the NWO graduate programme.

Appendix A. Equations solved

The expressions for the initial conditions in the simulations were generated from equation 5 using Mathematica. The source for the PENCIL-CODE is freely available on http://pencil-code.nordita.org/.

To simulate the plasma dynamics we assume an isothermal plasma, we take the background pressure to be the pressure for an isothermal gas $p = \rho c_s^2$, where ρ is the density and c_s^2 is the speed of sound squared. We solve the coupled equations in terms of $\boldsymbol{u}$, ρ, and $\boldsymbol{A}$, from which the magnetic field is calculated by $\boldsymbol{B} = \nabla \times \boldsymbol{A}$. The vector potential of the initial condition is calculated by $\boldsymbol{j} = \nabla \times \boldsymbol{B}$ and transforming that to the vector potential using the inverse Laplace transform.

The equation of motion for an isothermal plasma is

$$\frac{D\boldsymbol{u}}{Dt} = -c_s^2 \nabla \ln \rho + \boldsymbol{j} \times \boldsymbol{B}/\rho + \boldsymbol{F}_{\text{visc}} \tag{A.1}$$

where $\boldsymbol{u}$ is the fluid velocity, $\frac{D}{Dt} \equiv \frac{\partial}{\partial t} + \boldsymbol{u} \cdot \nabla$ is the convective derivative, and $\boldsymbol{j} = \nabla \times \boldsymbol{B}$. The viscous force is

$$\boldsymbol{F}_{\text{visc}} = \rho^{-1} \nabla \cdot 2\nu\rho \mathbf{S} \tag{A.2}$$

where ν is the kinematic viscosity and $\mathbf{S}$ is the traceless rate of strain tensor$S_{ij} = \frac{1}{2}(u_{i,j} + u_{j,i}) - \frac{1}{3}\delta_{ij} \nabla \cdot \boldsymbol{u}$. The continuity equation in terms of the logarithmic density has the form

$$\frac{D \ln \rho}{Dt} = -\nabla \cdot \boldsymbol{u}. \tag{A.3}$$

The induction equation can be written terms of the vector potential as

$$\frac{\partial \boldsymbol{A}}{\partial t} = \boldsymbol{u} \times \boldsymbol{B} + \eta \nabla^2 \boldsymbol{A} \tag{A.4}$$

where η is the magnetic diffusivity.

The PENCIL-code solves equations A.1, A.3, and A.4 using finite-difference methods to sixth-order in space and third-order in time. The simulation domain is a square box of size $(2\pi l_0)^3$ with 256^3 mesh points and open boundary conditions. Simulations with periodic boundary conditions were also performed, and seen to behave identically. The open boundary conditions are enforced by imposing vertical fields ($\boldsymbol{u}$, $\boldsymbol{B}$) at the boundary, allowing field to escape the simulation volume, and a constant first derivative of the density across the boundary.

All quantities are calculated using dimensionless units. The isothermal sound speed c_s, set is set to 1. The fluid velocity is set parallel to the magnetic field vector to satisfy equation 1, and the density is calculated from $\rho = p/c_s^2$ using the pressure from equation 3 with $p_\infty = 1$. The magnetic field is calculated from equation 5, with the constant c generally set to 0.25, but changed to a lower value if the simulation became unstable for the fields at higher values of n_t and n_p It was verified that time evolution is independent of this scaling. The fields were scaled to a characteristic length $r_0 = 1/2l_0$. The viscosity ν and magnetic diffusivity η were set to 2×10^{-4}.

Appendix B. Analysis of the zero lines

Here we analyze the null lines in the magnetic field of the initial plasma torus knots following refs. [34, 35].

From the field around the position of the null line we construct the matrix $\mathbf{M}$ with elements $M_{ij} = \partial_j B_i$ so that the magnetic field can be expressed to lowest order as

$$\boldsymbol{B} = \mathbf{M} \cdot \boldsymbol{r}, \tag{B.1}$$

where $\boldsymbol{r} = (x, y, z)^T$ is the position vector. The properties of the field around the zero points are now encoded in this matrix [35]. For example, the sum of the diagonal elements $\partial_j B_j$ is equal to the divergence of $\boldsymbol{B}$, thus the trace of the matrix is zero. The eigenvectors of this matrix determine three important directions in space. Since we are investigating the field on a zero line there is at least one direction where $\mathbf{M} \cdot \boldsymbol{r} = 0$, where the field remains zero. This is the eigenvector of the matrix $\mathbf{M}$ with eigenvalue zero. The other two eigenvectors have opposite eigenvalues, and (if the eigenvalues are real) determine the direction in space from which the field lines approach the null and in which direction the field lines leave the null, so that the field exhibits an x-point configuration.

We are interested in analyzing the null points of the plasma torus knots. We start with the expression for an (n_t, n_p) plasma torus knot given by equation (3) in the main paper. Without loss of generality we can ignore the rescaling and drop the numerical pre-factors $\sqrt{a}$ and c so that the expression for B_i in index notation is given by:

$$B_i = \mathrm{Im}\left[(n_t \alpha^{n_t - 1} n_p \beta^{n_p - 1}) \epsilon_{ijk} (\partial_j \alpha)(\partial_k \beta)\right] \tag{B.2}$$

where we use the two complex-valued Euler potentials given in equation 4

In the paper we describe how the magnetic field vanishes at points where α becomes zero if $n_t \neq 1$ and where β becomes zero if $n_p \neq 1$. These zeroes take the form of lines, with a zero line on the unit circle in the x, y-plane caused by the zero in α, and a straight zero line along the entire z-axis where β vanishes.

The element M_{ij} of the linearization matrix can be written using index notation as

$$\begin{aligned} M_{ij} = \partial_j B_i = \mathrm{Im}\left[n_t n_p \{(\partial_j \left[\alpha^{n_t-1}\beta^{n_p-1}\right]) (\epsilon_{ikl}(\partial_k\alpha)(\partial_l\beta))\right. \\ \left. +\alpha^{n_t}\beta^{n_p} (\partial_j(\epsilon_{ikl}(\partial_k\alpha)(\partial_l\beta))\}\right]. \end{aligned} \tag{B.3}$$

Because we are evaluating this field at a point where α respectively β vanish, the second term in equation B.3 is always zero. For the zero line on the unit circle (where $\alpha = 0$) the first term is only non-zero if the derivative of α^{n_t-1} is non-zero, and the same holds for β if we look at the zero line on the z-axis. Thus if $n_t \geq 3$ there are no non-zero elements in $\mathbf{M}$ around the unit circle, and if $n_p \geq 3$ this holds for $\mathbf{M}$ evaluated on the z-axis. All the matrix elements are zero because the field does not approach zero linearly.

Appendix B.1. Eigenvectors of the straight null

If we focus on the on the z-axis where $\beta = 0$, in the case that $n_p = 2$, the matrix elements become:

$$M_{ij}|_{\beta=0} = \mathrm{Im}\left[n_t n_p \alpha^{n_t-1} \partial_j \beta \boldsymbol{B}^i_{(1,1),\mathrm{compl}}\right] \tag{B.4}$$

where $\boldsymbol{B}_{(1,1),\mathrm{compl}} = \nabla\alpha \times \nabla\beta$, is the complex-valued vector field of the $(1, 1)$ plasma torus knot before taking the imaginary part. The linearization matrix on the z-axis becomes:

$$\mathbf{M} = n_t n_p \begin{pmatrix} \gamma & \delta & 0 \\ \delta & -\gamma & 0 \\ 0 & 0 & 0 \end{pmatrix}. \tag{B.5}$$

Where γ is given by:

$$\gamma = \frac{8\left(2z\cos\left(\arg\left((i+z)^2\right)(n_t-1)\right) + (z^2-1)\sin\left(\arg\left((i+z)^2\right)(n_t-1)\right)\right) n_p n_t}{(z^2+1)^4} \tag{B.6}$$

and δ is given by:

$$\delta = -\frac{8\left((z^2-1)\cos\left(\arg\left((i+z)^2\right)(n_t-1)\right) - 2z\sin\left(\arg\left((i+z)^2\right)(n_t-1)\right)\right) n_p n_t}{(z^2+1)^4} \tag{B.7}$$

The matrix $\mathbf{M}$ is symmetric, so the field around the null is characterized by three orthogonal eigenvectors, given by:

$$\boldsymbol{v}_1 = \begin{pmatrix} 0 \\ 0 \\ 1 \end{pmatrix}, \tag{B.8}$$

$$\boldsymbol{v}_2 = \begin{pmatrix} \frac{\gamma - \sqrt{\gamma^2+\delta^2}}{\delta} \\ 1 \\ 0 \end{pmatrix}, \tag{B.9}$$

$$\boldsymbol{v}_3 = \begin{pmatrix} \frac{\gamma+\sqrt{\gamma^2+\delta^2}}{\delta} \\ 1 \\ 0 \end{pmatrix}. \tag{B.10}$$

The respective eigenvalues are:

$$e_1 = 0, \tag{B.11}$$

$$e_2 = -\frac{8n_p n_t}{(z^2+1)^3}, \tag{B.12}$$

$$e_3 = \frac{8n_p n_t}{(z^2+1)^3}. \tag{B.13}$$

Here we have filled in the values of γ and δ.

The field around the z-axis is characterized by the null eigenvector in the z-direction indicating the direction of the null. The other two eigenvectors lie in the x, y-plane, with $\boldsymbol{v}_2$ determining the direction from which field lines approach the null line and $\boldsymbol{v}_3$ the direction in which field lines leave.

$\boldsymbol{v}_1$ and $\boldsymbol{v}_2$ are orthogonal in the x, y plane, and their direction depends on z. In order to determine the angle of these vectors in this plane as a function of z, we write the vector $\boldsymbol{v}_2$ as the complex number $\xi = \boldsymbol{v}_2^x + i\boldsymbol{v}_2^y$, where the superscripts denote the x- respectively the y-component of the vector. After some manipulation we get:

$$\xi = \frac{2}{e^{2i\arg(z+i)n_t} + i} + 2i \tag{B.14}$$

The only z-dependence is given by the term $\arg(z + i)$ in the exponent in the denominator. As z passes from $-\infty$ to ∞ the value of $\arg(i + z)$ varies smoothly from π to 0. This means that the value in exponent in the denominator varies from 0 to $2\pi n_t$. Each time that $2i\arg(z + i)n_t = n3\pi/4$, the denominator becomes zero, and the real part of ξ goes from ∞ to $-\infty$. This happens exactly n_t times, and the imaginary part of ξ remains constant. Thus, the argument of ξ, and therefore the angle of the vector $\boldsymbol{v_2}$ with the x-axis then rotates an angle of πn_t as z goes from $-\infty$ to ∞.

Since by virtue of the symmetry of the matrix $\mathbf{M}$ the vector $\boldsymbol{v}_3$ is orthogonal to $\boldsymbol{v}_2$, the two vectors rotate around the z-axis (and lie in the x, y-plane) in the same direction, making exactly $n_p/2$ full rotations as z goes from $-\infty$ to ∞. These two vectors determine the direction from which the field approaches and leaves the null, so the zero line is not a straightforward x-line, the directions from which field approach rotate, and the x-line null exhibits a twist over exactly $n_t\pi$ degrees.

Appendix B.2. Eigenvectors of the circular null

We now focus on the zero line on the unit circle in the x, y-plane that is present in the plasma torus knots when $n_t \neq 1$. This zero is characterized by the points where $\alpha = 0$. We choose the case where $n_t = 2$ so the expression for the linearization matrix becomes:

$$M_{ij}|_{\alpha=0} = \mathrm{Im}\left[n_t n_p \beta^{n_p-1}(\partial_j\alpha)\boldsymbol{B}^i_{(1,1),\mathrm{compl}}\right] \tag{B.15}$$

For this calculation we use cylindrical coordinates, as we know that the null line, and thus one of the eigenvectors of $\mathbf{M}$ is oriented along the unit circle in the x, y plane, in the ϕ-direction. The matrix $\mathbf{M}$ in this basis (r, ϕ, z) then becomes:

$$\mathbf{M} = n_p n_t \left(\begin{array}{ccc} \sin\left(\phi - \arg\left(e^{-i\phi}\right)(n_p - 1)\right) & 0 & -\cos\left(\phi - \arg\left(e^{-i\phi}\right)(n_p - 1)\right) \\ 0 & 0 & 0 \\ -\cos\left(\phi - \arg\left(e^{-i\phi}\right)(n_p - 1)\right) & 0 & -\sin\left(\phi - \arg\left(e^{-i\phi}\right)(n_p - 1)\right) \end{array} \right) \quad \text{(B.16)}$$

The three eigenvalues (in the (r, ϕ, z)-basis) are:

$$\boldsymbol{w}_1 = \left(\begin{array}{c} \sec\left(\phi - \arg\left(e^{-i\phi}\right)(n_p - 1)\right) - \tan\left(\phi - \arg\left(e^{-i\phi}\right)(n_p - 1)\right) \\ 0 \\ 1 \end{array} \right), \quad \text{(B.17)}$$

$$\boldsymbol{w}_2 = \left(\begin{array}{c} \left(1 + \sin\left(\phi - \arg\left(e^{-i\phi}\right)(n_p - 1)\right)\right)\left(-\sec\left(\phi - \arg\left(e^{-i\phi}\right)(n_p - 1)\right)\right) \\ 0 \\ 1 \end{array} \right), \quad \text{(B.18)}$$

$$\boldsymbol{w}_3 = \left(\begin{array}{c} 0 \\ 1 \\ 0 \end{array} \right), \quad \text{(B.19)}$$

where $\arg(\omega)$ denotes the argument of the complex number ω. The respective eigenvalues of these eigenvectors are

$$e_{c1} = -n_p n_t, \quad \text{(B.20)}$$

$$e_{c2} = n_p n_t \quad \text{(B.21)}$$

$$e_{c3} = 0. \quad \text{(B.22)}$$

The vector $\boldsymbol{w}_3$, with zero eigenvalue points in the ϕ-direction, the direction of the null line. The other two eigenvectors are perpendicular to that and orthogonal. We are again interested in the direction of these two vectors, as they determine the direction that field lines approach and leave the null.

We construct the complex number $\zeta = \boldsymbol{w}_1^r + i\boldsymbol{w}_1^z$ from the vector $\boldsymbol{w}_1$. After some manipulation we find:

$$\zeta = \frac{2}{e^{i\phi n_p} + i} + 2i \quad \text{(B.23)}$$

Now the argument of the complex number ζ is equal to the angle that the vector $\boldsymbol{w}_1$ makes with the r-vector, and it varies as a function of the angular coordinate ϕ in our cylindrical coordinate system. In a full rotation around the circular null, ϕ goes from 0 to 2π. The denominator of $\frac{2}{e^{i\phi n_p}+i}$ passes zero every time $i\phi n_p = 3\pi/4$, which is exactly n_p times. This takes the real part of ζ from ∞ to $-\infty$ n_p times, whilst the imaginary part remains constant. Thus, the argument of ζ, and therefore the angle that the vector $\boldsymbol{w}_1$ makes with the r-vector in the r, z-plane makes a rotation of an angle of exactly $n_p\pi$ in a full pass around the circular null.

The vector $\boldsymbol{w}_2$ is orthogonal to $\boldsymbol{w}_1$, and they signify the direction that field lines approach and leave the null. Also the circular null exhibits a twisted x-point geometry, with the direction of field line approach and the direction of field line departure rotating an angle of $n_p\pi$ over the length of the null line.

[1] Urbantke H 2003 *Journal of geometry and physics* **46** 125–150

[2] Chen B G g, Ackerman P J, Alexander G P, Kamien R D and Smalyukh I I 2013 *Physical review letters* **110** 237801

[3] Monastyrsky M I 2007 *Topology in molecular biology* (Springer)

[4] Ran Y, Hosur P and Vishwanath A 2011 *Physical Review B* **84** 184501

[5] Volovik G E and Mineev V P 1977 *Sov. Phys. JETP* **46** 401–404

[6] Kawaguchi Y, Nitta M and Ueda M 2008 *Physical Review Letters* **100** 180403

[7] Hall D S, Ray M W, Tiurev K, Ruokokoski E, Gheorghe A H and Möttönen M 2016 *Nature Physics*

[8] Dzyloshinskii I E and Ivanov B A 1979 *Journal of Experimental and Theoretical Physics* **29** 540–542

[9] Rañada A F 1989 *Letters in Mathematical Physics* **18** 97–106

[10] Irvine W T M and Bouwmeester D 2008 *Nature Physics* **4** 716–720

[11] Hoyos C, Sircar N and Sonnenschein J 2015 *Journal of Physics A: Mathematical and Theoretical* **48** 255204

[12] Smiet C, Candelaresi S, Thompson A, Swearngin J, Dalhuisen J and Bouwmeester D 2015 *Physical Review Letters* **115** 095001

[13] Kamchatnov A M 1982 *Sov. Phys. JETP* **55** 69–73

[14] Taylor J B 1974 *Physical Review Letters* **33** 1139

[15] Moffatt H K 1969 *Journal of Fluid Mechanics* **35** 117–129

[16] Woltjer L 1958 *Proceedings of the National Academy of Sciences of the United States of America* **44** 833

[17] Hornig G and Schindler K 1996 *Physics of Plasmas (1994-present)* **3** 781–791

[18] Hopf H 1931 *Mathematische Annalen* **104** 637–665

[19] Chandrasekhar S 1956 *Proceedings of the National Academy of Sciences* **42** 273–276

[20] Kapur J and Jain R 1961 *Zeitschrift fur Astrophysik* **52** 110

[21] Moffatt H 2015 *Journal of Plasma Physics* **81** 905810608

[22] Kedia H, Bialynicki-Birula I, Peralta-Salas D and Irvine W M T 2013 *Physical Review Letters* **111** 150404

[23] Thompson A, Wickes A, Swearngin J and Bouwmeester D 2015 *Journal of Physics A: Mathematical and Theoretical* **48** 205202

[24] Thompson A, Swearngin J, Wickes A and Bouwmeester D 2014 *Physical Review E* **89** 043104

[25] Bateman H 1915 *The Mathematical Analysis of Electrical and Optical Wave-motion on the Basis of Maxwell's Equations* (Cambridge: Cambridge University Press) ISBN 9781163966525

[26] Berger M and Field G B 1984 *Journal of Fluid Mechanics* **147** 133–148

[27] Berger M A 1999 *Plasma Physics and Controlled Fusion* **41** B167

[28] Brandenburg A and Dobler W 2002 *Computer Physics Communications* **147** 471–475

[29] Haugen N E L, Brandenburg A and Dobler W 2004 *Physical Review E* **70** 016308

[30] Scheeler M W, Kleckner D, Proment D, Kindlmann G L and Irvine W T 2014 *Proceedings of the National Academy of Sciences* **111** 15350–15355

[31] Hudson S, Dewar R, Dennis G, Hole M, McGann M, von Nessi G and Lazerson S 2012 *Physics of Plasmas (1994-present)* **19** 112502

[32] Shafranov V 1958 *Soviet Phys. JETP* **6**

[33] Bialynicki-Birula I 2004 *Journal of Optics A: Pure and Applied Optics* **6** S181

[34] Lau Y T and Finn J M 1990 *The Astrophysical Journal* **350** 672–691

[35] Parnell C, Smith J, Neukirch T and Priest E 1996 *Physics of Plasmas (1994-present)* **3** 759–770

[36] Pontin D 2011 *Advances in Space Research* **47** 1508–1522

[37] Greene J M 1988 *Journal of Geophysical Research: Space Physics (1978–2012)* **93** 8583–8590

[38] Brasselet J P, Seade J and Suwa T 2009 *Vector fields on singular varieties* vol 1987 (Springer Science & Business Media)

[39] Grad H 1961 Containment in cusped plasma systems Tech. rep. New York Univ., New York. Inst. of Mathematical Sciences

[40] Krall N A 1992 *Fusion Science and Technology* **22** 42–49
[41] Wakatani M 1998 *Stellarator and Heliotron devices* 95 (Oxford University Press)

Acknowledgements

I am grateful for the the support of the Quantum Optics group. Especially prof. Bouwmeester and (now) dr. Smiet, for both the great opportunity to work on a real paper, as the incredible patience they have had to see this project and thesis to it's final conclusion.

References

[1] E. A. Fredricksmeyer, *Alexander, Midas, and the Oracle at Gordium*, Classical Philology **56**, 160 (1961).

[2] H. K. Moffatt, *The degree of knottedness of tangled vortex lines*, Journal of Fluid Mechanics **35**, 117–129 (1969).

[3] B. G.-g. Chen, P. J. Ackerman, G. P. Alexander, R. D. Kamien, and I. I. Smalyukh, *Generating the Hopf Fibration Experimentally in Nematic Liquid Crystals*, Phys. Rev. Lett. **110**, 237801 (2013).

[4] A. F. Rañada, *A topological theory of the electromagnetic field*, Letters in Mathematical Physics **18**, 97 (1989).

[5] W. T. Irvine and D. Bouwmeester, *Linked and knotted beams of light*, Nature Physics **4**, 716 (2008).

[6] C. Hoyos, N. Sircar, and J. Sonnenschein, *New knotted solutions of Maxwell's equations*, Journal of Physics A: Mathematical and Theoretical **48**, 255204 (2015).

[7] L. H. Kauffman, *Knots and physics*, volume 1, World scientific, 2001.

[8] G. P. Collins, *Computing with Quantum Knots*, Scientific American **294**, 56 (2006).

[9] R. Edgeworth, B. J. Dalton, and T. Parnell, *The pitch drop experiment*, European Journal of Physics **5**, 198 (1984).

[10] G. Călugăreanu, *Sur les classes d'isotopie des noeuds tridimensionnels et leurs invariants*, Czechoslovak Mathematical Journal **11**, 588 (1961).

[11] W. A. Newcomb, *Motion of magnetic lines of force*, Annals of Physics **3**, 347 (1958).

[12] S. Chandrasekhar, *On force-free magnetic fields*, Proceedings of the National Academy of Sciences **42**, 1 (1956).

[13] R. Lüst and A. Schlüter, *Kraftfreie Magnetfelder. Mit 4 Textabbildungen*, Zeitschrift fur Astrophysik **34**, 263 (1954).

Version of June 26, 2018– Created June 26, 2018 - 13:50

[14] J. P. Freidberg, *Ideal MHD*, Cambridge University Press, 2014.

[15] S. Chandrasekhar, *On the stability of the simplest solution of the equations of hydromagnetics*, Proceedings of the National Academy of Sciences **42**, 273 (1956).

[16] T. J. M. Boyd and J. J. Sanderson, *The Physics of Plasmas.*, Cambridge University Press, 2003.

[17] *The Pencil-Code: a high-order finite-difference code for compressible MHD*, 2014.

[18] Z. Wang, J. Si, W. Liu, and H. Li, *Equilibrium and magnetic properties of a rotating plasma annulus*, Physics of Plasmas **15**, 102109 (2008).

[19] H. Kedia, I. Bialynicki-Birula, D. Peralta-Salas, and W. M. T. Irvine, *Tying knots in light fields*, Physical Review Letters **111**, 150404 (2013).

[20] H. Bateman, *The Mathematical Analysis of Electrical and Optical Wave-motion on the Basis of Maxwell's Equations*, Cambridge University Press, Cambridge, 1915.

[21] I. Robinson, *Null Electromagnetic Fields*, Journal of Mathematical Physics **2**, 290 (1961).

[22] A. F. Rañada, *A topological theory of the electromagnetic field*, letters in mathematical physics **18**, 97 (1989).

[23] A. Thompson, J. Swearngin, A. Wickes, and D. Bouwmeester, *Constructing a class of topological solitons in magnetohydrodynamics*, Physical Review E **89**, 043104 (2014).

[24] S. R. Hudson, R. L. Dewar, G. Dennis, M. J. Hole, M. McGann, G. von Nessi, and S. Lazerson, *Computation of multi-region relaxed magnetohydrodynamic equilibria*, Physics of Plasmas **19**, 112502 (2012).

[25] C. B. Smiet, S. Candelaresi, A. Thompson, J. Swearngin, J. W. Dalhuisen, and D. Bouwmeester, *Self-Organizing Knotted Magnetic Structures in Plasma*, Phys. Rev. Lett. **115**, 095001 (2015).

[26] D. Pontin, *Three-dimensional magnetic reconnection regimes: A review*, Advances in Space Research **47**, 1508 (2011).

[27] P. F. Wyper and R. Jain, *Reconnection at three dimensional magnetic null points: Effect of current sheet asymmetry*, Physics of Plasmas **20**, 052901 (2013).

[28] V. S. Titov, E. Tassi, and G. Hornig, *Exact solutions for steady reconnective annihilation revisited*, Physics of Plasmas **11**, 4662 (2004).

[29] C. Smiet, A. Thompson, P. Bouwmeester, and D. Bouwmeester, *Magnetic surface topology in decaying plasma knots*, New Journal of Physics **19**, 023046 (2017).

Version of June 26, 2018– Created June 26, 2018 - 13:50